Simultaneous disruption of PRC2 and enhancer function underlies histone H3.3-K27M oncogenic activity in human hindbrain neural stem cells

Gerard L. Brien[1,5*], Raul Bardini Bressan[2,3,4,5], Craig Monger[1,5], Dáire Gannon[1], Eimear Lagan[1], Anthony M. Doherty[1], Evan Healy[1], Hannah Neikes[1], Darren J. Fitzpartrick[1], Orla Deevy[1], Vivien Grant[2,3], Maria-Angeles Marqués-Torrejón[2,3], Neza Alfazema[2,3], Steven M. Pollard[2,3*] and Adrian P. Bracken[1*]

Affiliations

1. Smurfit Institute of Genetics, Trinity College Dublin, Dublin 2, Ireland.
2. Cancer Research UK Edinburgh Centre, University of Edinburgh, Edinburgh, United Kingdom.
3. Centre for Regenerative Medicine, University of Edinburgh, Edinburgh, United Kingdom.
4. Biotech Research and Innovation Centre, University of Copenhagen, Copenhagen 2200, Denmark
5. These authors contributed equally.

* Co-corresponding authors: Gerard Brien (brieng@tcd.ie); Steven Pollard (steven.pollard@ed.ac.uk); Adrian Bracken (adrian.bracken@tcd.ie).

Abstract

Driver histone H3-K27M mutations are frequent in pediatric midline brain tumors. However, the precise mechanisms by which H3-K27M causes tumor initiation remain unclear. Here, we use human hindbrain neural stem cells to model the consequences of H3.3-K27M on the epigenomic landscape in a relevant developmental context. Genome-wide mapping of epitope-tagged histone H3.3 reveals that both wildtype and K27M-mutant incorporate abundantly at pre-existing active enhancers and promoters, and to a lesser extent at PRC2-bound regions. At active enhancers, H3.3-K27M leads to focal H3K27ac loss, decreased chromatin accessibility, and reduced transcriptional expression of nearby neurodevelopmental genes. In addition, H3.3-K27M deposition at a subset of PRC2 target genes leads to increased PRC2 and PRC1 binding and augmented transcriptional repression that can be partially reversed by PRC2 inhibitors. Our work suggests that rather than imposing *de novo* transcriptional circuits, H3.3-K27M drives tumorigenesis by locking initiating cells in their pre-existing, immature epigenomic state, via disruption of PRC2 and enhancer functions.

Introduction

Diffuse midline gliomas (DMG) are universally fatal childhood brain tumors with median survival of less than one year[1,2]. The majority (~80%) of these tumors harbor a somatic, heterozygous mutation in *H3F3A* or *HIST1H3B*, which encode histone H3 proteins, resulting in a lysine-to-methionine substitution at position 27 (K27M)[3,4]. The most common mutations occur in *H3F3A*, which encodes the histone H3 variant, H3.3. Unlike the canonical histones H3.1/2, H3.3 incorporates into chromatin in a replication-independent manner at specific loci, including active gene promoters, enhancers and heterochromatic regions[5-7]. *H3F3A* K27M mutations arise early in gliomagenesis and are frequently accompanied by secondary mutations in *TP53* and *PDGFRA*[8-10]. Consistent with this, H3.3-K27M cooperates with *TP53* loss and *PDGFRA* activation to drive DMG-like tumor development *in vivo*[11,12]. H3-K27M mutations are now considered pathognomonic of a disease entity defined by the World Health Organization as 'diffuse midline glioma, H3 K27M-mutant', which includes tumors previously referred to as diffuse intrinsic pontine glioma (DIPG), and other diffuse high-grade gliomas arising in the brainstem, thalamus and spinal cord[13].

As the K27M mutation occurs at a critical regulated site in H3, it was presumed to alter the epigenomic landscape and interfere with gene expression control[1,14]. Indeed, initial characterization of H3K27M-mutant patient samples and cell lines revealed global changes in the abundance of post-translational modifications at H3K27[15]. This residue can be mono-, di- and tri-methylated (H3K27me1/2/3) by Polycomb Repressive Complex 2 (PRC2) or acetylated (H3K27ac) by CBP/p300[16,17]. Notably, while the K27M mutant histone typically accounts for <10% of total histone H3 in tumor cells, its presence leads to a 70-90% reduction in the global levels of H3K27me2 and H3K27me3[15,18,19]. This is associated with an approximately 2-fold increase in global H3K27ac levels[15]. Biochemical studies established that PRC2 has a higher binding affinity for K27M-mutant nucleosomes and that K27M can inhibit PRC2 enzymatic activity[15,20,21]. This led to the proposal of the so-called PRC2 sequestration model, where the complex would become bound and inactivated at sites of abundant H3K27M incorporation[22]. However, recent work demonstrated that deposition of H3-K27M in chromatin is not required to reduce H3K27me2/3 levels[23]. This, together with the fact several studies have shown H3K27me3 is retained focally at PRC2-bound regions in K27M mutant cells[18,19,24,25], indicates the oncohistone does not inactivate PRC2 on

chromatin. Moreover, how H3K27M influences the deposition of H3K27ac remains unclear with conflicting reports indicating that K27M directly stimulates H3K27ac at discrete genomic sites or indirectly across broad genomic windows[26,27]. As such, there is a need for clarity on how H3K27M influences the regulatory processes that converge on H3K27 during the earliest stages of tumor development.

Here, we examined the direct impact of H3.3-K27M in human fetal hindbrain neural stem cells (NSCs) – an anatomically and developmentally relevant, isogenic system, to better model the etiology of H3.3-K27M DMGs. We isolated and engineered primary hindbrain NSCs expressing epitope-tagged H3.3, enabling the comparative genome-wide mapping of K27M and its wild-type counterpart. We found that the point mutation does not alter the genome-wide distribution of H3.3. However, H3.3-K27M directly augments Polycomb-mediated repression of a cohort of PRC1/2-bound neurodevelopmental genes. Surprisingly, despite broad increases of H3K27ac across the genome, correlating with reductions in H3K27me2/3, incorporation of H3.3-K27M at tissue specific enhancers leads to focal reductions in both H3K27ac and chromatin accessibility with consequential reductions in expression of nearby neurodevelopmental genes. Finally, by screening a set of small-molecule inhibitors targeting several chromatin regulators, we found PRC2 inhibition preferentially blocks the growth of H3.3-K27M mutant cells, reversing aberrant repression of PRC2 target genes. We propose that H3.3-K27M directly impairs the ability of hindbrain NSCs to activate transcriptional networks required for differentiation.

Results

An isogenic human hindbrain NSC model of K27M mutant disease

Histone H3 mutations show unique temporal and regional specificity, with the majority of H3.3-K27M tumors arising within hindbrain regions[8,28]. We therefore reasoned that human NSCs derived from the fetal hindbrain would represent a developmentally relevant model to investigate the role of H3.3-K27M. Supporting this, we recently demonstrated that human fetal hindbrain NSC cultures recapitulate defining transcriptional features of primary K27M-mutant tumors and, as opposed to forebrain-derived NSCs, are sensitized to H3.3-K27M oncogenic activity[29]. Therefore, we used this model to dissect the transcriptional and epigenomic consequences of H3.3-K27M during early stages of gliomagenesis by stably expressing epitope-tagged H3.3 (wild-type or K27M) in hindbrain NSC cultures from two independent human fetal specimens (GCGR-NS19 and GCGR-NS13; see Methods) (Fig. 1a and Extended Data Fig. 1a). Absolute quantifications of wild-type and K27M-mutant transgenes showed the exogenous histones are expressed at similar levels to endogenous *H3F3A* (Extended Data Fig. 1b). Moreover, immunoblots with an anti-H3.3 specific antibody showed the exogenous V5-tagged H3.3 accounts for ~30-50% of total histone H3.3 levels (Extended Data Fig. 1c). Immunoblotting with an antibody recognizing total histone H3 demonstrated the exogenous H3.3 proteins represent ~0.5% of total H3 (Extended Data Fig. 1d). These data confirm the exogenous H3.3 proteins are expressed at an appropriate physiological level for this cellular context. As expected, expression of H3.3-K27M led to global reductions in H3K27me2/3 accompanied by increased H3K27ac (Fig. 1b). Functionally, expression of H3.3-K27M promoted an elevated growth rate, accompanied by down-regulation of PRC2 target and tumor suppressor gene, *CDKN2A*/p16 (Extended Data Fig. 1e-g), whose increased repression is a downstream consequence of K27M in tumors[25,30].

To further assess the relevance of these hindbrain NSCs as a tumor-initiation model, we engineered two additional genetic abnormalities, commonly associated with H3.3-K27M[8] – i.e. *PDGFRA* overexpression and *TP53* loss-of-function in wild-type H3.3 (PP5W) and K27M-mutant (PP5K) NSC cultures. Compared to PP5W, H3.3-K27M expressing PP5K cultures exhibited an elevated growth rate and/or increased colony forming activity, as well as reduced SA-β-galactosidase positivity (Extended Data Fig.

2a-c). Upon stereotactic injection into immunocompromised mice, PP5K cells induced tumor formation with a shorter latency than PP5W cells, which is in agreement with previously reported mouse models[12,25,31] (Extended Data Fig. 2d). Grafted cells displayed a diffuse, infiltrating pattern in mouse tissue akin to histological features seen in DMG patients (Extended Data Fig. 2e-f). Consistent with the shorter tumor latency, PP5K tumors had a significantly higher proliferation index than PP5W cells (Extended Data Fig. 2g), underscoring the disease relevance of this isogenic hindbrain NSC model.

Next, we assessed global gene expression changes induced by H3.3-K27M and found a relatively broad transcriptional response, with 728 up- and 1,140 down-regulated genes (Extended Data Fig. 3a). Consistent with the K27M mutation being an early event in gliomagenesis, H3.3-K27M alone was sufficient to initiate a tumor-associated gene expression signature in hindbrain NSCs (Extended Data Fig. 3b-c). Taken together, these data demonstrate our fetal hindbrain NSC model recapitulates important transcriptional, biochemical, and clinical aspects of H3.3-K27M mutant midline gliomas, underscoring its relevance to study the early stages of DMG development.

K27M does not alter the distribution of histone H3.3

To study the initial consequences of the H3.3-K27M oncogene on the chromatin landscape of hindbrain NSCs, we assessed its impact in the absence of additional mutations. To determine whether the K27M mutation alters the distribution of H3.3, we performed extensive characterization of the chromatin landscape in NSCs expressing wild-type or K27M-mutant H3.3. This demonstrated a close correlation in the genome-wide distribution of wildtype and K27M H3.3 (Fig. 1c and Extended Data Fig. 3d). This confirmed the K27M mutation does not dramatically alter the localization of H3.3 in hindbrain NSCs and that H3.3-K27M is not incorporated at *de novo* chromatin regions.

Next, we performed genome-wide correlations between ChIP-seq of V5-tagged wild-type and K27M-mutant H3.3, and exogenous reference genome normalized ChIP-seq (ChIP-Rx) of PRC2 member SUZ12, PRC1 member BMI1, and the H3K27me2, H3K27me3, H3K27ac, H3K4me1 and H3K4me3 histone post-translational

modifications. Both wild-type and K27M-mutant H3.3 clustered closest to H3K27ac (Fig. 1d), consistent with prior observations H3.3 is most abundant at active euchromatic regions[5]. To gain a more detailed overview of the localization of wild-type and K27M-mutant H3.3, we defined three sets of genomic regions based on our ChIP-Rx data; (1) Active promoters, defined by a H3K27ac peak overlapping a promoter region; (2) Active enhancers, defined by H3K27ac peaks distal to promoters and (3) PRC2 target promoters, defined by SUZ12 peaks overlapping promoters (Fig. 1e-f). Both wild-type and K27M-mutant H3.3 were most abundantly incorporated at active enhancers and slightly less at active promoters (Fig. 1e and Extended Data Fig. 3e-f). This is consistent with the fact the genome-wide localization of wild-type and K27M-mutant H3.3 correlate more closely with enhancer-associated H3K4me1, compared to promoter-specific H3K4me3 (Fig. 1d). Both wild-type and K27M H3.3 were enriched at PRC2 target promoters, albeit at lower levels and not at an additional set of repressed (non-PRC2 target) loci (Fig. 1f and Extended Data Fig. 3f), consistent with previous mapping of wild-type H3.3 in mouse embryonic stem cells (ESCs)[32]. These data demonstrate that, like wild-type H3.3, the majority of H3.3-K27M is at active enhancers and promoter regions, and to a lesser extent at PRC2 target regions.

Aberrant repression of a cohort of PRC2 target loci

Despite the increased binding affinity of PRC2 for K27M-containing nucleosomes, our data demonstrate H3.3-K27M deposition in chromatin is not sufficient to sequester PRC2 to active enhancers or promoters (Fig. 1e; see lack of SUZ12 signal on “Active enhancers” and “Active promoters”). To explore whether H3.3-K27M alters Polycomb binding at other genomic regions, we divided the genome into approximately 300,000 10-kb bins, quantified SUZ12 and BMI1 ChIP-Rx signal within each bin and then compared the signal between wild-type and K27M NSCs (Fig. 2a). This revealed that SUZ12 and BMI1 binding increased at a cohort of pre-existing Polycomb target regions, which already had high levels of PRC2 and PRC1 in wild-type H3.3 NSCs (Fig. 2a-b). Consistent with this, although several SUZ12 peaks (867) were identified only in K27M NSCs, these sites had robust, albeit lower, levels of SUZ12 binding in H3.3 wild-type NSCs, confirming they are not *de novo* binding sites (Extended Data Fig. 4a). This demonstrates that the presence of H3.3-K27M is associated with increased PRC1/2 binding at a cohort of pre-existing Polycomb target sites (Extended Data Fig. 4b). Supporting this, quantification of SUZ12 read densities outside existing

peaks provided no evidence for *de novo* PRC2 binding in K27M cells (Extended Data Fig. 4c).

To determine where PRC2 binding increases occur, we ranked PRC2 target promoters based on changes in SUZ12 abundance between wild-type and K27M NSCs (Fig. 2b). This generated three categories of PRC2 target promoters – those gaining SUZ12 (>1.5-fold; 307), those with unchanged SUZ12 (± 0.1-fold; 277) and those with reduced SUZ12 (>1.5-fold; 136). Promoters that gained SUZ12 largely retained H3K27me3 and had increased levels of BMI1 (Fig. 2b-c and Extended Data Fig. 4b). Consistent with the higher binding affinity of PRC2 for K27M, promoters gaining SUZ12 had relatively higher levels of H3.3-K27M incorporation (Fig. 2b). Moreover, the SUZ12 peaks identified only in K27M NSCs also had relatively higher levels of H3.3-K27M (Extended Data Fig. 4a). Furthermore, the 307 Polycomb target promoters gaining SUZ12 (>1.5-fold) had higher CpG densities and lower H3K4me3 levels compared to other SUZ12-bound regions (Fig. 2b and Extended Data Fig. 4d-e)[19].

A previous report suggested PRC2 can become sequestered at poised enhancer elements in H3.3-K27M-expressing mESCs[33]. Using our ChIP-Rx datasets, we defined poised enhancer regions (263) in hindbrain NSCs, based on positivity for H3K27me3 and H3K4me1, and the absence of H3K4me3 and H3K27ac[34] (Extended Data Fig. 4f). This revealed that SUZ12 binding did increase on poised enhancers, coincident with H3.3-K27M incorporation (Extended Data Fig. 4f). Importantly, these sites are pre-existing PRC2-bound regions in hindbrain NSCs, rather than *de novo* SUZ12 binding sites. Taken together, these data indicate H3.3-K27M incorporation is not sufficient to induce *de novo* PRC2 binding but can lead to increased PRC2 and PRC1 abundance at a subset of previously bound sites, including Polycomb target genes and poised enhancers.

Next, we examined the relationship between changes in SUZ12 binding at promoters and gene expression. This identified a significant negative correlation between changes in SUZ12 abundance and transcriptional dynamics (Fig. 2d). Remarkably, functional analysis of the 307 genes with increased SUZ12 revealed a striking enrichment of gene ontology (GO) terms related to neurodevelopmental biology (Fig.

2e). In contrast, the remaining Polycomb target genes with unchanged or reduced SUZ12 were not enriched for neurodevelopmental regulators (Extended Data Fig. 5a). Furthermore, genes with promoters gaining SUZ12 had significantly reduced mRNA levels in K27M mutant NSCs, whereas the genes with unchanged or reduced SUZ12 binding did not (Fig. 2f and Extended Data Fig. 5b). These data indicate that PRC2 and PRC1 binding increases at a cohort of neurodevelopmental gene promoters, coincident with high H3.3-K27M incorporation, leading to their aberrant repression.

Focal losses of H3K27ac despite widespread global increases

Next, we wanted to quantify the global dynamics of H3K27 modifications in H3.3-K27M mutant NSCs. Despite the 90% reduction in H3K27me3 (Fig. 1b), comparable peak numbers exist in wild-type (3,080) and K27M-mutant (3,193) NSCs (Extended Data Fig. 6a). This is consistent with studies showing H3K27me3 is retained at PRC2-bound regions in K27M-mutant cells[18,19,23-25]. To explore this further, we quantified the proportion of H3K27me3 that exists at and outside PRC2-bound sites. To do this, we separated the genome into three categories based on H3K27me3 distribution; (1) Targeted regions, corresponding to SUZ12-bound sites; (2) Background regions, corresponding to H3K27ac peaks; and (3) Dispersed regions, comprising the rest of the genome. All three categories of H3K27me3 distribution are exemplified at the *HOXA* locus (Fig. 3a). After quantifying ChIP-Rx read densities for SUZ12 and H3K27me3 at Targeted and Dispersed regions, we found only a minority of H3K27me3 reads (~2%) map within Targeted regions, while the majority are found at Dispersed genomic sites (Fig. 3b and Extended Data Fig. 6b). Therefore, in wild-type NSCs, the majority of H3K27me3 is present outside PRC2-bound sites and, like H3K27me2, is deposited without stable PRC2 binding[17,35]. Quantitative analysis of H3K27me3 dynamics demonstrated the modification is reduced by ~25% at PRC2-bound regions and ~75% at Dispersed regions (Fig. 3b). Furthermore, H3K27me2, like H3K27me3, is primarily lost across broad genomic regions (Fig. 3c and Extended Data Fig. 6c-e).

Quantitative ChIP-Rx analyses demonstrate the global increases in H3K27ac occur across broad genomic windows (Fig. 3c). These increases are coincident with loss of H3K27me2/3, suggesting reduced methylation leads to increased H3K27ac (Extended Data Fig. 6f). Supporting this, we observed similar changes in *Ezh2* heterozygous knock-out mESCs, where H3K27ac increases are broadly coincident with loss of

H3K27me2/me3 (Extended Data Fig. 6g). Intriguingly, despite the widespread gain of H3K27ac in K27M-mutant NSCs, we detected no evidence of *de novo* peak formation and in fact observed fewer H3K27ac peaks in K27M-mutant NSCs (Fig. 3d).

To gain a broader view of H3K27ac dynamics, we compared ChIP-Rx read densities across the ~300,000 10-kb bins in wild-type and K27M-mutant NSCs (Fig. 3e and Extended Data Fig. 6h). Strikingly, this revealed many genomic regions with high H3K27ac in wild-type NSCs have reduced levels in K27M-mutant cells (Fig. 3e and Extended Data Fig. 6h; see highlighted regions). In contrast, the same analyses in *Ezh2* heterozygous mESCs showed H3K27ac levels increase across all genomic regions (Extended Data Fig. 6h). Upon closer inspection, we noticed most genomic bins have very low levels of H3K27ac and in K27M-mutant NSCs, H3K27ac predominantly increases within these regions (Fig. 3e and Extended Data Fig. 6h; see 'Low abundance regions'). We expect that despite the modest increases in H3K27ac per individual bin, the fact they collectively account for most of the genome likely explains the 2-fold global increase in H3K27ac global levels observed in K27M-mutant NSCs (Fig. 1b and Extended Data Fig. 6i). Together, these data indicate that while loss of dispersed H3K27me2/3 correlate with and are likely causative of broad increases of H3K27ac, in H3.3-K27M expressing cells, H3K27ac is reduced at regions where the modification is abundant in wild-type cells.

H3K27M incorporation at enhancers disrupts regulatory functions

Next, we sought to determine whether direct H3.3-K27M incorporation at active promoter and enhancer regions leads to reductions in H3K27ac and explore the downstream consequences on gene expression. We identified approximately 41% fewer H3K27ac peaks in K27M-mutant compared to wild-type NSCs (Fig. 4a). Interestingly, we observed a greater reduction in the number of H3K27ac peaks at enhancers (62% fewer) compared to promoters (22% fewer) (Fig. 4b). Consistent with this, analysis of enhancer landscapes revealed a marked reduction in the total number of both typical and super enhancers (Fig. 4c and Extended Data Fig. 7a-b). Moreover, in addition to there being fewer active enhancers in K27M-mutant NSCs, those that remained had comparatively lower levels of H3K27ac than in WT cells (Fig. 4c and Extended Data Fig. 7c). Consistent with the preferential disruption of enhancer elements, H3K27ac losses were more pronounced at enhancers compared to

promoters (Fig. 4d and Extended Data Fig. 7c-e). Remarkably, at both promoter and enhancer regions, higher levels of H3.3-K27M incorporation were linked to greater losses of H3K27ac (Extended Data Fig. 7f-g). To understand if this feature is unique to H3.3-K27M, we examined data from a recent study that expressed H3.1-K27M or H3.3-K27M in ESC-derived derived oligodendrocyte progenitor cells (OPCs)[36]. This demonstrated that both oncohistones induced losses of H3K27ac at active regulatory regions (Fig. 4e-f). Consistent with the idea that the incorporation of K27M at these sites directly contributes to H3K27ac losses, both H3.1 and H3.3-K27M are enriched at active promoters and enhancers in primary DMG samples (Extended Data Fig. 7h). Taken together, these data indicate that deposition of H3-K27M disrupts the deposition of H3K27ac at promoters and enhancers in our primary hindbrain NSC disease model and in patient-derived cell lines.

To examine whether the incorporation of H3.3-K27M alters the function of regulatory elements, we measured chromatin accessibility using the assay for transposase accessible chromatin, coupled with sequencing (ATAC-seq)[37]. This demonstrated greater accessibility changes at enhancers compared to promoters (Extended Data Fig. 8a), consistent with the preferential disruption of enhancers in K27M-mutant NSCs. Remarkably, despite the comparable numbers of enhancers gaining and losing accessibility, the transcriptional changes were primarily associated with accessibility losses (Fig. 4g). Indeed, many genes associated with enhancers that lost accessibility and H3K27ac were downregulated, while those near enhancers with reduced H3K27ac and increased accessibility had unchanged expression (Fig. 4g). Of note, GO analyses of genes with nearby enhancers losing both H3K27ac and accessibility in K27M-mutant NSCs revealed a striking enrichment of terms related to nervous system development and neural differentiation, while those with unchanged accessibility lacked such enrichment (Extended Data Fig. 8b-c). These data suggest that H3.3-K27M causes an impairment of neurodevelopmental enhancer function, which leads to the decreased expression of nearby genes associated with neural differentiation (Fig. 4h and Extended Data Fig. 8b). Taken together, these data indicate H3.3-K27M disrupts the function of active regulatory regions, including gene enhancers, likely contributing to oncogenesis by hindering NSC differentiation, which is a general feature of pediatric brain tumors[38].

EZH2 inhibition reverses changes mediated by H3.3-K27M

Several studies have highlighted the clinical potential of therapeutic molecules targeting chromatin regulators in K27M-mutant DMGs[25,26,39,40]. We wanted to evaluate the specificity of these therapeutic approaches using our isogenic system, which we reasoned would facilitate the identification of therapeutic vulnerabilities specifically linked to H3.3-K27M (Fig. 5a). We examined the response of PP5W (wild-type H3.3) and PP5K (H3.3-K27M) cultures to treatment with molecules targeting transcriptional activators (BET family members, CDK7 and CBP/p300) and repressors (PRC2 and HDAC enzymes). Two independent EZH2 inhibitors showed selectivity against PP5K cells, while other compounds did not elicit differential responses based on K27M status (Fig. 5b and Extended Data Fig. 9a). These data suggest that K27M cells are preferentially susceptible to EZH2 inhibitors, while the potency of the other compounds does not appear to be linked to K27M.

We next wondered whether PRC2 inhibitor treatment could reverse the aberrant transcriptional repression of PRC2 targets in H3.3-K27M mutant NSCs (Fig. 2d-f and Extended Fig. 5b), thereby potentially explaining the specific sensitivity of K27M mutant NSCs. To explore this, we examined transcriptional changes following PRC2 inhibition using RNA-seq of matched cultures treated with the EZH2 inhibitor Tazemetostat (also known as EPZ6438) or DMSO for 9 days (Fig. 5c). We observed a greater number of up-regulated genes in K27M-mutant PP5K, compared to PP5W cultures following PRC2 inhibition. In contrast, similar numbers of down-regulated genes were observed in both lines. GO analyses demonstrated that very similar gene sets were upregulated in response to EZH2 inhibition in both PP5W and PP5K cultures (Extended Data Fig. 9b). The up-regulated genes were enriched for terms related to development and differentiation, while downregulated genes were primarily associated with cell cycle regulation (Extended Data Fig. 9b). Interestingly, genes with increased SUZ12 binding at their promoters in H3.3-K27M-expressing NSCs (Fig. 2b), were more upregulated in PP5K than PP5W cultures (Fig. 5d). Gene expression data from a previously published study demonstrated that mouse homologs of these SUZ12-gained genes were also preferentially upregulated following Tazemetostat treatment of a mouse NSC model of K27M-mutant DMG (Extended Data Fig. 9c)[25]. Moreover, shRNA-mediated knockdown of SUZ12 in an established K27M-mutant DMG cell line led to upregulation of SUZ12-gained genes (Extended Data Fig. 9c)[26].

Together, these data indicate that genes gaining SUZ12 at their promoters in K27M-mutant NSCs are actively repressed by PRC2, and sensitive to targeting of the complex. This highlights PRC2 inhibition can reverse the aberrant transcriptional repression of these loci in K27M-mutant NSCs (Fig. 2f). Furthermore, a broader set of PRC2 target genes were found to be more responsive to PRC2 inhibition in K27M-mutant NSCs (Fig. 5d). All three subsets of SUZ12 target genes (Gained/Unchanged/Reduced) increased significantly in expression in PP5K, compared to PP5W cells following Tazemetostat treatment (Fig. 5d-e), while repressed non-PRC2 target genes are unaffected (Extended Data Fig. 9d). A previous study linked the therapeutic response to PRC2 inhibitor treatment in K27M-mutant DMG to activation of the *CDKN2A*/p16 tumor suppressor[25]. We find that *CDKN2A*/*INK4A* expression is activated to comparable levels in both PP5W and PP5K cultures (Extended Data Fig. 9e; see *INK4A* specific exon), despite the difference in therapeutic response (Fig. 5b). This indicates that *INK4A* activation is not the only contributing factor to the observed phenotypic effects in K27M-mutant NSCs, which are likely driven by the broad de-repression of PRC2 targets. This highlights a clear therapeutic vulnerability in H3.3-K27M mutant cells where PRC2 target loci are more sensitive to PRC2 inhibition (Fig. 5e and Extended Data Fig. 9f).

Finally, we examined expression of the neurodevelopmental regulatory genes associated with enhancers losing H3K27ac and chromatin accessibility, which were downregulated in K27M-mutant NSCs (Extended Data Fig. 8b). These genes were only modestly upregulated in Tazemetostat-treated PP5K cultures (Extended Data Fig. 9g), suggesting this may be an indirect effect and other targeted approaches may be required to fully activate these genes. Importantly, while the acute (24 h) treatment of K27M-mutant DMG cell lines with JQ1 (BET bromodomains), THZ1 (CDK7) or Panobinostat (HDACs) elicit very broad transcriptional changes, Tazemetostat has a more discrete effect on transcription (Fig. 5c and Extended Data Fig. 10). This indicates that while JQ1, THZ1 and Panobinostat are potent against K27M-mutant DMG cells, this may be the result of widespread, non-specific effects on transcription, as opposed to targeting specific underlying disease mechanisms. Therefore, our data indicate PRC2 inhibition may represent a more specific, mechanistically anchored therapeutic approach in DMGs with H3.3-K27M.

Discussion

To study the initial consequences of H3.3-K27M on the chromatin landscape in a disease relevant context, we developed an isogenic model of DMG using human fetal hindbrain NSCs. By quantitatively mapping PRC1 and PRC2, as well as H3K27 and H3K4 modifications, and integrating these data with ATAC- and RNA-seq analyses, we demonstrate that the H3.3-K27M oncohistone directly impairs the developmental potential of hindbrain NSCs by augmenting PRC2 repression of a cohort of neurodevelopmental genes and disrupting tissue-specific enhancer function (Fig. 6).

Understanding how H3.3-K27M influences PRC2 function has been an active area of research for several years. Here, we establish that incorporation of H3.3-K27M is not sufficient to sequester PRC2. We find no evidence for *de novo* PRC2 binding at regions with high levels of H3.3-K27M incorporation in hindbrain NSCs. We show that active enhancer and promoter regions with the highest levels of H3.3-K27M incorporation lack PRC2 binding. Therefore, it is unlikely that the higher affinity of PRC2 for H3.3-K27M mutant nucleosomes is sufficient to drive its relocation. We have, however, provided evidence that in certain contexts H3.3-K27M incorporation at existing PRC2-bound regions leads to elevated SUZ12 binding. Intriguingly, this occurs at a subset of neurodevelopmental gene promoters with high CpG density and low levels of H3K4me3, as well as some poised enhancers. Together, these findings indicate that the increased affinity between PRC2 and H3.3-K27M leads to increased PRC2 retention at certain chromatin regions, but that the oncohistone is not sufficient to recruit PRC2. Rather, it is likely that other factors such as the Polycomb-like and JARID2 accessory proteins are the key mediators of PRC2 localization in both wild-type and H3.3-K27M expressing NSCs[41-43].

Several studies have shown that H3K27me3 peaks persist at PRC2-bound sites, despite the overall reduction of this modification in K27M-mutant cells[18,19,24,25]. Consistent with this, our quantitative analyses demonstrated that only a minority of H3K27me3 losses occur at peak regions. Instead, H3K27me3, like H3K27me2, is primarily lost across broad chromatin domains outside PRC2-bound regions. This is consistent with recent evidence that H3.3-K27M primarily inhibits PRC2-mediated

H3K27me3 in *trans*[23,24]. Preferential binding of allosterically activated PRC2 by K27M appears to impede the global spreading of H3K27me2/3 from PRC2-bound regions[21,23,44]. It is unclear if this broadly dispersed H3K27 methylation is functional, and it will be important to examine this since there are clear implications for understanding K27M-mutant gliomagenesis and the underlying biology of PRC2. Of note, we found that losses of broad H3K27me2/3 are concomitant with global increases in H3K27ac, suggesting this is a consequence of the vastly increased pool of non-methylated H3K27 in K27M-mutant NSCs, providing additional substrate for p300/CBP. While it is unclear if these global, non-directed increases in H3K27ac contribute to tumor development, they may have clinical relevance. Recent evidence suggests the associated increases of transcription from repetitive DNA elements may, at least in part, explain sensitivity to DNA demethylating agents and HDAC inhibitors[27].

The ability to map the distribution of K27M and wild-type H3.3, in an isogenic human model also allowed us to discover that tissue-specific enhancers are directly disrupted by the oncohistone. Chromatin mapping of H3.3-K27M has proven challenging, with only a limited number of studies reporting global mapping of H3-K27M distribution[26,33,36]. Moreover, no studies to date have mapped H3.3-K27M distribution in a disease relevant, isogenic model system, which has hampered attempts to understand its function. Our model, exploiting an epitope tag and robust ChIP reagents, allowed us to observe abundant deposition of H3.3-K27M at enhancer regions leading to reduced H3K27ac at these regulatory elements. To explore if the global increases in H3K27ac are caused by ‘leeching’ of H3K27 acetyltransferase activity from enhancers and promoters, we developed an independent model system (mESCs lacking one *Ezh2* allele) with similarly reduced H3K27me2/3 and increased H3K27ac levels. This revealed that despite the broad increases of H3K27ac across the genome in these cells, the modification is not decreased at enhancers and promoters. This supports our proposal that the reductions in H3K27ac in H3.3-K27M expressing cells are due to direct incorporation of H3.3-K27M. Moreover, by examining published datasets[36], we found that H3.1-K27M also reduces H3K27ac at these regions corresponding to its enriched deposition at these sites. This may be because K27M-mutant H3 histones cannot serve as a productive substrate for p300/CBP-mediated H3K27 acetylation. Interestingly, despite losses of H3K27ac at essentially all enhancers, we did not observe a strong global effect on gene

expression. Rather, we find a preferential downregulation of neurodevelopmental genes whose enhancer regions lose both H3K27ac and chromatin accessibility. This indicates that loss of H3K27ac alone is not sufficient to impair enhancer function, consistent with findings that ablating H3K27ac at enhancers in mESCs did not disrupt gene regulation[45]. It also implies that gene expression changes in this cohort of genes are not the reason for reduced H3K27ac at their enhancers and promoter regions. Furthermore, it indicates these important developmental gene regulatory elements are uniquely susceptible to perturbation by H3.3-K27M. Therefore, it remains important to explore the functional consequences of H3.3-K27M incorporation at neurodevelopmental enhancers, and in the context of H3.1-K27M.

Finally, we used our isogenic model to test the selectivity of molecules targeting various chromatin regulators. A key unmet need in DMG with H3.3-K27M is the provision of effective, mechanistically anchored therapeutic approaches. While studies have demonstrated K27M-mutant glioma cell lines are sensitive to treatment with molecules targeting chromatin regulatory proteins, including EZH2, HDAC enzymes, BET bromodomain family members and CDK7[25,26,39,40]; without engineered isogenic models it is challenging to understand whether their potency is linked to the presence of K27M. Here, we provide compelling evidence that the potency of PRC2 inhibitors is linked to the K27M mutation. Other molecules tested did not selectively target K27M-expressing cells and appear to broadly disrupt transcriptional regulation. In contrast, PRC2 inhibitors elicit a more discreet transcriptional response, while reversing changes induced in K27M-mutant cells (Fig. 6a). Our data also highlight that identifying approaches that reverse the impairment of neurodevelopmental gene enhancer function may provide an additional mechanistically anchored therapeutic approach (Fig. 6b). Therefore, it remains important to rationally screen using pharmacological and genomic approaches for additional therapeutic vulnerabilities specific to H3-K27M mutant cells. We propose that the ability to functionally characterize specific vulnerabilities in an isogenic system will provide important insights on approaches that disrupt the direct effects of oncohistones.

Our work indicates that H3.3-K27M initiates cancer development by focally augmenting PRC2 repression and impairing enhancer control of discreet sets of

neurodevelopmental regulatory genes. Moreover, we have shown that PRC2 inhibition reverses at least some of the direct pathogenic effects mediated by H3.3-K27M. Taken together, our data support the idea that H3.3-K27M is the critical early driver in DMGs, aberrantly locking self-renewing hindbrain NSCs in their immature epigenomic state prior to accumulation of mutations that drive cell proliferation and survival.

References

1. Mohammad, F. & Helin, K. Oncohistones: drivers of pediatric cancers. *Genes Dev* **31**, 2313-2324 (2017).
2. Jones, C. & Baker, S.J. Unique genetic and epigenetic mechanisms driving paediatric diffuse high-grade glioma. *Nat Rev Cancer* **14**(2014).
3. Wu, G. *et al.* Somatic histone H3 alterations in pediatric diffuse intrinsic pontine gliomas and non-brainstem glioblastomas. *Nat Genet* **44**, 251-3 (2012).
4. Schwartzentruber, J. *et al.* Driver mutations in histone H3.3 and chromatin remodelling genes in paediatric glioblastoma. *Nature* **482**, 226-31 (2012).
5. Goldberg, A.D. *et al.* Distinct factors control histone variant H3.3 localization at specific genomic regions. *Cell* **140**, 678-91 (2010).
6. Talbert, P.B. & Henikoff, S. Histone variants on the move: substrates for chromatin dynamics. *Nat Rev Mol Cell Biol* **18**, 115-126 (2017).
7. Maze, I., Noh, K.M., Soshnev, A.A. & Allis, C.D. Every amino acid matters: essential contributions of histone variants to mammalian development and disease. *Nat Rev Genet* **15**, 259-71 (2014).
8. Mackay, A. *et al.* Integrated Molecular Meta-Analysis of 1,000 Pediatric High-Grade and Diffuse Intrinsic Pontine Glioma. *Cancer Cell* **32**, 520-537 e5 (2017).
9. Vinci, M. *et al.* Functional diversity and cooperativity between subclonal populations of pediatric glioblastoma and diffuse intrinsic pontine glioma cells. *Nat Med* **24**, 1204-1215 (2018).
10. Nikbakht, H. *et al.* Spatial and temporal homogeneity of driver mutations in diffuse intrinsic pontine glioma. *Nat Commun* **7**, 11185 (2016).
11. Pathania, M. *et al.* H3.3(K27M) Cooperates with Trp53 Loss and PDGFRA Gain in Mouse Embryonic Neural Progenitor Cells to Induce Invasive High-Grade Gliomas. *Cancer Cell* **32**, 684-700 e9 (2017).
12. Larson, J.D. *et al.* Histone H3.3 K27M Accelerates Spontaneous Brainstem Glioma and Drives Restricted Changes in Bivalent Gene Expression. *Cancer Cell* **35**, 140-155 e7 (2019).
13. Louis, D.N. *et al.* The 2016 World Health Organization Classification of Tumors of the Central Nervous System: a summary. *Acta Neuropathol* **131**, 803-20 (2016).
14. Weinberg, D.N., Allis, C.D. & Lu, C. Oncogenic Mechanisms of Histone H3 Mutations. *Cold Spring Harb Perspect Med* **7**(2017).
15. Lewis, P.W. *et al.* Inhibition of PRC2 activity by a gain-of-function H3 mutation found in pediatric glioblastoma. *Science* **340**, 857-61 (2013).
16. Bracken, A.P., Brien, G.L. & Verrijzer, C.P. Dangerous liaisons: interplay between SWI/SNF, NuRD, and Polycomb in chromatin regulation and cancer. *Genes Dev* **33**, 936-959 (2019).
17. Conway, E., Healy, E. & Bracken, A.P. PRC2 mediated H3K27 methylations in cellular identity and cancer. *Curr Opin Cell Biol* **37**, 42-8 (2015).
18. Chan, K.M. *et al.* The histone H3.3K27M mutation in pediatric glioma reprograms H3K27 methylation and gene expression. *Genes Dev* **27**, 985-90 (2013).

19. Bender, S. *et al.* Reduced H3K27me3 and DNA hypomethylation are major drivers of gene expression in K27M mutant pediatric high-grade gliomas. *Cancer Cell* **24**, 660-72 (2013).
20. Justin, N. *et al.* Structural basis of oncogenic histone H3K27M inhibition of human polycomb repressive complex 2. *Nat Commun* **7**, 11316 (2016).
21. Diehl, K.L. *et al.* PRC2 engages a bivalent H3K27M-H3K27me3 dinucleosome inhibitor. *Proc Natl Acad Sci U S A* **116**, 22152-22157 (2019).
22. Voigt, P. & Reinberg, D. Putting a halt on PRC2 in pediatric glioblastoma. *Nat Genet* **45**, 587-9 (2013).
23. Jain, S.U. *et al.* H3 K27M and EZHIP Impede H3K27-Methylation Spreading by Inhibiting Allosterically Stimulated PRC2. *Mol Cell* **80**, 726-735 e7 (2020).
24. Harutyunyan, A.S. *et al.* H3K27M induces defective chromatin spread of PRC2-mediated repressive H3K27me2/me3 and is essential for glioma tumorigenesis. *Nat Commun* **10**, 1262 (2019).
25. Mohammad, F. *et al.* EZH2 is a potential therapeutic target for H3K27M-mutant pediatric gliomas. *Nat Med* **23**, 483-492 (2017).
26. Piunti, A. *et al.* Therapeutic targeting of polycomb and BET bromodomain proteins in diffuse intrinsic pontine gliomas. *Nat Med* **23**, 493-500 (2017).
27. Krug, B. *et al.* Pervasive H3K27 Acetylation Leads to ERV Expression and a Therapeutic Vulnerability in H3K27M Gliomas. *Cancer Cell* **35**, 782-797 e8 (2019).
28. Sturm, D. *et al.* Hotspot mutations in H3F3A and IDH1 define distinct epigenetic and biological subgroups of glioblastoma. *Cancer Cell* **22**, 425-37 (2012).
29. Bressan, R.B. *et al.* Regional identity of human neural stem cells determines oncogenic responses to histone H3.3 mutants. *Cell Stem Cell* (2021).
30. Bracken, A.P. *et al.* The Polycomb group proteins bind throughout the INK4A-ARF locus and are disassociated in senescent cells. *Genes Dev* **21**, 525-30 (2007).
31. Cordero, F.J. *et al.* Histone H3.3K27M Represses p16 to Accelerate Gliomagenesis in a Murine Model of DIPG. *Mol Cancer Res* **15**, 1243-1254 (2017).
32. Banaszynski, L.A. *et al.* Hira-dependent histone H3.3 deposition facilitates PRC2 recruitment at developmental loci in ES cells. *Cell* **155**, 107-20 (2013).
33. Fang, D. *et al.* H3.3K27M mutant proteins reprogram epigenome by sequestering the PRC2 complex to poised enhancers. *Elife* **7**(2018).
34. Rada-Iglesias, A. *et al.* A unique chromatin signature uncovers early developmental enhancers in humans. *Nature* **470**, 279-83 (2011).
35. Ferrari, K.J. *et al.* Polycomb-dependent H3K27me1 and H3K27me2 regulate active transcription and enhancer fidelity. *Mol Cell* **53**, 49-62 (2014).
36. Nagaraja, S. *et al.* Histone Variant and Cell Context Determine H3K27M Reprogramming of the Enhancer Landscape and Oncogenic State. *Mol Cell* **76**, 965-980 e12 (2019).
37. Corces, M.R. *et al.* An improved ATAC-seq protocol reduces background and enables interrogation of frozen tissues. *Nat Methods* **14**, 959-962 (2017).
38. Jessa, S. *et al.* Stalled developmental programs at the root of pediatric brain tumors. *Nat Genet* **51**, 1702-1713 (2019).
39. Nagaraja, S. *et al.* Transcriptional Dependencies in Diffuse Intrinsic Pontine Glioma. *Cancer Cell* **31**, 635-652 e6 (2017).

40. Grasso, C.S. *et al.* Functionally defined therapeutic targets in diffuse intrinsic pontine glioma. *Nat Med* **21**, 555-9 (2015).
41. Glancy, E., Ciferri, C. & Bracken, A.P. Structural basis for PRC2 engagement with chromatin. *Curr Opin Struct Biol* **67**, 135-144 (2020).
42. Healy, E. *et al.* PRC2.1 and PRC2.2 Synergize to Coordinate H3K27 Trimethylation. *Mol Cell* **76**, 437-452 e6 (2019).
43. Hojfeldt, J.W. *et al.* Non-core Subunits of the PRC2 Complex Are Collectively Required for Its Target-Site Specificity. *Mol Cell* **76**, 423-436 e3 (2019).
44. Stafford, J.M. *et al.* Multiple modes of PRC2 inhibition elicit global chromatin alterations in H3K27M pediatric glioma. *Sci Adv* **4**, eaau5935 (2018).
45. Zhang, T., Zhang, Z., Dong, Q., Xiong, J. & Zhu, B. Histone H3K27 acetylation is dispensable for enhancer activity in mouse embryonic stem cells. *Genome Biol* **21**, 45 (2020).

Acknowledgements

We thank members of the Bracken, Pollard and Brien laboratories for helpful discussions and critical reading of the manuscript. We are grateful to the Genomics Core at University College Dublin for expertise and help with next-generation sequencing. Work in the Bracken laboratory is supported by the Worldwide Cancer Research and The Brain Tumour Charity (18-0592), the Irish Research Council Advanced Laureate Award (IRCLA/2019/21), the Health Research Board (HRB-ILP-POR-2017-078), Science Foundation Ireland under the SFI Investigators (SFI/16/IA/4562) and BBSRC-SFI (SFI/17/BBSRC/3415) Programmes, the Irish Cancer Society (CancersUnmetNeeds012) and the St. Vincent's Foundation. O.D. was supported by a PhD fellowship from the Irish Research Council Government of Ireland Postgraduate Scholarship Programme (GOIPG/2017/2009). D.G. was supported by a PhD fellowship from the Irish Research Council Government of Ireland Postgraduate Scholarship Programme (GOIPG/2019/2084). R.B.B. was supported by a fellowship from the Science Without Borders Program (CAPES, Governo Dilma Rousseff, Brazil) and a postdoctoral fellowship from EMBO. S.M.P. was supported by a Cancer Research UK Senior Research Fellowship (A17368). S.M.P. and R.B.B. were supported by a project grant from Children with Cancer (15/189). Support for cellular models was provided by Gillian Morrison and the Cancer Research UK-funded Centre Accelerator Award (A21922) (http://gcgr.org.uk). Work in the Brien laboratory is supported by a Science Foundation Ireland Starting Investigator Research Grant (18/SIRG/5573), an Irish Cancer Society Biomedical Research Fellowship (CRF18BRI) and a Worldwide Cancer Research grant (21-0271).

Author Contributions

G.L.B., R.B.B., S.M.P. and A.P.B. conceived the project and designed the experiments. R.B.B., V.G. and S.M.P. derived and engineered the human fetal hindbrain NSCs cultures. G.L.B. performed most of the bench-based experimentation, while R.B.B. and D.G. contributed to phenotypic characterizations of NSC cultures. E.L. performed EZH2 inhibitor treatment and global gene expression analyses in DIPGXIII cells. O.D. performed ESC ChIP-RX analyses. R.B.B., M.-A.M.-T. and N.A. performed the xenotransplantation experiments. C.M., H.N., A.M.D., E.H. and D.J.F. performed the bioinformatic analyses. G.L.B., R.B.B., D.G. and A.P.B. co-wrote the manuscript with contributions from all other authors.

Declaration of Interests

S.M.P. is a founder and shareholder of Cellinta Ltd., a biotechnology start-up that is developing cancer therapeutics. He is also a paid consultant to Cellinta Ltd. S.M.P. is an inventor on a University of Edinburgh patent related to neural stem cell culture methods (WO2005121318A3). The other authors declare no competing interests.

Figure Legends for main text figures

Fig. 1: The K27M mutation does not alter the genome-wide localization of histone H3.3

a. Schematic overview of the isogenic experimental model. Human fetal neural stem cells (NSCs) derived from the hindbrain regions of 2 independent embryos (GCGR-NS19 and GCGR-NS13) were used to establish cultures expressing wild-type (WT) or K27M-mutant H3.3.

b. Immunoblot analyses for the indicated H3K27 modifications in cell lysates derived from biological duplicate NSC lines expressing WT or K27M-mutant H3.3 (left panel). Quantifications of H3K27 modification abundance in the presented immunoblotting experiments (right panel), (*n = 2* biologically independent samples).

c. Genomic tracks showing H3.3 WT and K27M (V5) ChIP-seq signal in GCGR-NS19 NSCs on the entire chromosome 8 (top tracks) or the region encompassing chr8:12,720,000-37,000,000 on the p arm of the chromosome, bottom tracks (top panel). Genome-wide correlations of H3.3 WT and K27M (V5) ChIP-seq read densities in NSCs derived from embryo GCGR-NS19. The correlation coefficient for the two conditions is indicated (bottom panel).

d. Heatmaps representing the genome-wide correlations between each of the identified ChIP samples in H3.3 WT (left panel) and K27M-mutant (right panel) expressing NSC cultures.

e. Tornado plots showing averaged enrichments for the indicated ChIP-seq/ChIP-Rx experiments in biological duplicate H3.3-K27M-expressing NSC cultures. Indicated are regions corresponding to ±10 kb genomic windows around PRC2 target promoters, Active Enhancers and Active Promoters.

f. Meta-plots of average H3.3-K27M ChIP-seq enrichment in biological duplicate experiments in genomic windows ±10 kb of Active Promoter, Active Enhancer, PRC2 target promoters and non-PRC2 target Repressed gene promoters.

Fig. 2: H3.3-K27M deposition at the promoters of PRC2 target genes leads to increased PRC1/2 binding and augmented gene repression

a. Schematic representation of the genome-wide quantitative ChIP-Rx approach, separating the genome into ~300,000 individual 10-kb bins (left), and genome-wide correlations of SUZ12 ChIP-Rx read densities in genome-wide bins between WT and K27M-mutant NSC cultures (embryo GCGR-NS19) (right).

b. Heatmap presenting the fold-change in SUZ12 binding at PRC2 target promoters in WT and K27M-mutant NSC cultures. Also indicated are the 3 categories of PRC2 targets – those gaining SUZ12 binding (>1.5-fold, 307), those with unchanged SUZ12 (± 0.1-fold, 277) and those with reduced SUZ12 binding (>1.5-fold, 136) (Left). Meta tracks showing ChIP-Rx (SUZ12, H3K27me3 and BMI1) and ChIP-seq (V5-H3.3) normalized read densities ± 10 kb of Polycomb target gene promoters at sites gaining, losing and with unchanged SUZ12 binding in K27M-mutant NSC cultures, as per the left panel.

c. Genomic tracks showing averaged SUZ12, H3K27me3 and BMI1 ChIP-Rx and H3.3-K27M ChIP-seq signals from biological duplicate experiments at the indicated genomic locus hindbrain NSC cultures (chr4:112,474,873-112,554,822).

d. Correlation plots demonstrating the relationship between changes in SUZ12 binding at the promoter regions of all PRC2 target genes, and changes in mRNA levels for the same genes. *P* value and correlation coefficient were calculated using Pearson correlation.

e. Gene ontology analysis of genes with gained (>1.5-fold) SUZ12 binding in K27M-mutant NSC cultures.

f. Box plots presenting the fold-change in gene expression as measured by RNA-seq for genes in the three categories highlighted in panel b, $n = 4$ biologically independent samples. *P* values were calculated using an unpaired two-sided *t*-test. Box plots present median and interquartile range with whiskers encompassing minimum and maximum data values.

Fig. 3: Losses of H3K27me2/3 broadly throughout the genome correlate with global increases in H3K27ac

a. Genomic tracks showing averaged H3K27me3, SUZ12 and H3K27ac ChIP-Rx signal at the indicated genomic locus (chr7:26,811,403-27,600,402) in WT and K27M-mutant NSC cultures. Also indicated are representative example regions of the three categories of H3K27me3 deposition used in downstream analyses. 'Targeted' regions represent PRC2-bound regions, 'Background' regions correspond to H3K27ac peaks and 'Dispersed' regions correspond to the remainder of the genome.

b. Bar charts presenting the number of ChIP-Rx normalized read counts for SUZ12 (left) and H3K27me3 (right) present within 'Targeted' and 'Dispersed' regions in H3.3 WT NSC GCGR-NS19 (top panel). Bar charts presenting the dynamic shifts in H3K27me3 ChIP-Rx normalized read counts within 'Targeted' and 'Dispersed' regions (bottom panel), *n = 2* biologically independent samples.

c. Rolling average plots presenting the fold-change of the indicated H3K27 modifications in quantitative ChIP-Rx comparisons across the entire chromosome 8 in hindbrain NSC cultures from embryo GCGR-NS19.

d. Venn diagrams presenting the total numbers and overlap of identified H3K27ac peak sets in WT and K27M-mutant hindbrain NSC cultures (top panel). Meta-tracks presenting quantitative ChIP-Rx normalized H3K27ac signal at overlapping and distinct peak sets identified by Venn diagram analysis (bottom panels).

e. Genome-wide correlations of H3K27ac ChIP-Rx read densities in WT and K27M conditions in embryo GCGR-NS19 (left panel). Correlations of H3K27ac ChIP-Rx read densities in WT and K27M conditions as per left panel, specifically in low abundance regions (right panel).

Fig. 4: Impaired activity of neurodevelopmental gene enhancers in K27M-mutant hindbrain NSCs.

a. Bar charts presenting the relative shift in H3K27ac peak numbers between WT and K27M-mutant hindbrain NSC cultures. The total number of peaks identified in each condition are indicated on the x-axis.

b. Bar charts presenting the relative shift in H3K27ac peak numbers between WT and K27M-mutant hindbrain NSC cultures at active promoters (left) and enhancer elements (right). The total number of peaks identified in each condition are indicated on the x-axes.

c. Ranked Order of Super Enhancer (ROSE) analysis in WT and K27M-mutant NSC cultures for embryo GCGR-NS19.

d. Genomic tracks of the *SOX9* locus (chr17:72,096,279-72,177,233) showing averaged H3K27ac, H3K4me3 and H3K4me1 ChIP-Rx, H3.3-K27M ChIP-seq and ATAC-seq in WT and K27M-mutant hindbrain NSC cultures. The chromosome 17 ideogram is displayed above the gene tracks with the relevant region highlighted.

e. Meta tracks of H3K27ac ChIP-seq signal at active promoter and enhancer regions in oligodendrocyte progenitor cells (OPCs) before (-Dox) and after (+Dox) induction of H3.3-K27M (left) or H3.1-K27M (right) expression. Data taken from Nagaraja et al. 2019.

f. Genomic tracks of the *SOX9* locus (chr17:72,096,279-72,177,233) showing H3K27ac ChIP-seq signal in OPC culture as per panel e.

g. Box plots presenting changes in gene expression levels for genes adjacent to enhancer elements losing or gaining chromatin accessibility (ATAC-seq) in H3.3-K27M mutant NSC cultures, $n = 4$ biologically independent samples. Box plots present median and interquartile range with whiskers encompassing minimum and maximum data values.

h. Box plots presenting expression value for the indicated neurodevelopmental genes in hindbrain NSC cultures with WT or K27M H3.3, $n = 4$ biologically independent samples.

Fig. 5: EZH2 inhibitor treatment reverses oncogenic transcriptional repression in K27M mutant cells

a. Schematic presentation of compound screening experiments using isogenically matched PP5W and PP5K hindbrain NSC cultures.

b. Cellular viability dose-response data in PP5W (black) or PP5K (red) cultures treated with the indicated small-molecule compounds, *n = 2* biologically independent samples. Data are presented as mean values ± SEM

c. RNA-seq volcano plot presenting the gene expression changes observed in PP5W (left) and PP5K (right) NSC lines treated with 2 mM Tazemetostat for 9-days. Red and blue denotes genes significantly up and down-regulated, respectively in each culture. Indicated are the total numbers of up/down regulated genes, and number of up/down regulated genes among those gaining SUZ12 binding at their promoters.

d. Box plots presenting the log_2 fold-change in gene expression for all genes gaining, with unchanged or reduced SUZ12 binding in Tazemetostat treated PP5W or PP5K cultures, *n = 3* biologically independent samples. Box plots present median and interquartile range with whiskers encompassing minimum and maximum data values.

e. Box plots presenting log_2 expression values for each of the indicated genes in H3.3 WT or K27M mutant NSCs (top panel) or PP5K cells treated with DMSO or Tazemetostat for 9 days (bottom panel), *n = 3* biologically independent samples. Box plots present median and interquartile range with whiskers encompassing minimum and maximum data values.

Fig. 6: Direct effects of H3.3-K27M in human fetal hindbrain neural stem cells.

a. Schematic representation of the direct changes elicited by H3.3-K27M at PRC2 target sites in human hindbrain NSCs. Deposition of H3.3-K27M at a subset of PRC2 target gene promoters which leads to increased PRC2 binding and greater gene repression. However, these effects can be reversed by treating cells with EZH2 inhibitory drugs.

b. Abundant deposition of H3.3-K27M at gene enhancers limits the deposition of H3K27ac at these elements resulting in downregulation of neurodevelopmental gene expression programs. Currently, it is unclear if these effects can be therapeutically reversed/manipulated. However, therapeutic approaches targeting regulators of enhancer biology may provide a means to disrupt the effects of K27M at these sites.

Methods

Cell Culture

Human GCGR-NS19 and GCGR-NS13 cell lines were provided by the Glioma Genetics Resource (www.gcgr.org.uk). The cell lines were derived from the brainstem region of 19- and 13.5-week-old human fetuses, respectively, as previously described[29]. Participants provided informed consent after reading an information sheet about the research (Investigation of key regulatory processes in tissue and stem cell development) and were not compensated financially. The fetal samples were obtained after elective termination of pregnancy. These procedures received ethical approval from the NHS Health Research Authority (South East Scotland Research Ethics Committee, REC reference 08/S1101/1). The region of interest was dissected from whole brain tissue, collected in ice-cold PBS and mechanically dissociated by trituration. Samples were further dissociated with Accutase enzyme mixture at 37°C for 5 min, filtered using a 70-µm strainer and centrifuged at 400g for 5 min. The resulting cell pellet was resuspended in culture medium and plated onto a T25 tissue culture flask. Established lines were propagated in serum-free basal medium supplemented with N2 and B27 (Life Technologies), Laminin-1 (R&D Systems, 2-4 µg/ml) and growth factors EGF and FGF2 (Peprotech, 10 ng/ml) as previously described[46]. Medium was refreshed every 3-4 days and cells were split 1:3 upon dissociation with Accutase solution (Sigma) once a week. HSJD-DIPG-007 and HSJD-DIPG-021 patient-derived DIPG cell lines were a kind gift from A.M. Carcabosa, while DIPGXIII were kindly provided by N. Jabado and grown as monolayers in Tumor Stem Media (TSM) composed of 50% DMEM/F12, 50% Neurobasal-A medium, supplemented with 1% HEPES 1 M, 1% MEM Non-essential amino acids, 1% 100 mmol/l sodium pyruvate, 1% GlutaMAX, 2% B27 without vitamin A (all from Life Technologies), 20 ng/ml human EGF, 20 ng/ml human bFGF, 10 ng/ml human PDGF-AA, 10 ng/ml human PDGF-BB (all from Peprotech), 5 IU/ml heparin (Sigma) and Laminin-1 (R&D Systems, 2-4 µg/ml).

Plasmids

Human H3F3A expression vectors were generated by engineering a Gateway cloning destination vector containing the PiggyBac transposase inverted repeats flanking a

CAG promoter-driven transcriptional unit and a PGK-Hygromycin selection cassette. The sequences encoding V5-tagged wild-type and K27M mutant H3.3 were generated by commercial DNA synthesis (Life Technologies). These were flanked by AttL recombination sites, and directly inserted into the destination vector via Gateway LR cloning. PDGFRA overexpression plasmid was generated through PCR amplification of human *PDGFRA* cDNA followed by Gateway cloning into a PiggyBac compatible destination vector. Human *TP53* CRISPR sgRNA and targeting vectors were previously described[47].

Cell transfection

Human fetal hindbrain NSCs were engineered at 4-5 passages after establishment. Transfections were performed using the Amaxa 4D nucleofection system as previously described[47]. For ectopic H3.3 expression, 200 ng of piggybac donor vector (wild-type or K27M-mutant H3.3) were co-transfected with 400 ng of transposase vector PBase. For combined PDGFRA expression and TP53 knockout, PDGFRA donor vector (200 ng), TP53 sgRNA (200 ng), *TP53*-targeting vector (200 ng), Cas9-encoding plasmid (400 ng) were added to the reaction. Following recovery, cells were selected for stable integration of PiggyBac donor vectors and *TP53*-targeting vector using sequential treatment with 50 µg/ml hygromycin (H3.3), 5 µg/ml blastidicin (PDGFRa) and 100 ng/ml puromycin (TP53 knockout). The resulting resistant cell population was expanded for 3-4 passages before the functional assays and genome-wide profiling experiments. For transplantation experiments, cells were transfected with the Luciferase-2A-GFP piggybac vector and labelled cells enriched by FACS.

SA-βGal staining

Cells were fixed in solution containing 2% formaldehyde and 0.2% glutaraldehyde for 5 min and stained overnight with the Senescence Cells Histochemical Staining kit (Sigma) according to manufacturer's instructions. Plates were imaged using phase contrast microscopy and positive cells manually quantified from a total ~2,000 cells in a minimum of ten random fields.

EdU incorporation and colony formation assays

For EdU incorporation, cells were plated at 5,000 cells/cm^2 in 48-well plates for 72 h, followed by incubation with 10 μM EdU for 24 h. EdU staining was carried out using the Click-iT EdU Alexa Fluor 647 assay kit (Life Technologies) according to manufacturer's instructions. EdU-positive cells were quantified from a total ~5,000 cells in a minimum of ten random fields. Total cell number was determined by DAPI nuclear staining. For colony formation assays, cells were plated at 15 cells/cm^2 in 6-well plates, and colony numbers counting manually determined 21 days after plating.

Cell Growth Analysis

H3.3 wild-type or K27M-mutant NSCs were seeded (75,000 cells/well) in biological triplicate in 6-well plates and cultured for a subsequent 5 days. Cells were counted in each well at 5-day intervals and the cumulative cell number calculated before re-seeding 75,000 cells/well.

Xenotransplantation

Xenotransplantation experiments were performed as previously described[48]. Briefly, cells were detached with Accutase, pelleted, and diluted at 100,000 cells per microliter in sterile PBS. Two microliters of the cell solution were injected stereotactically into the striatum of 6- to 8-week-old male NSG mice under general anesthesia. Animals were maintained and used in accordance with protocols approved by The University of Edinburgh Animal Welfare and Ethical Review Body (AWERB) and the UK Government Home Office, under a project license issued to S.M.P. (PC0395462) at the University of Edinburgh. Animals were observed regularly until they became moribund or showed severe neurological symptoms, at which point they were sacrificed, and the presence of intracranial tumors confirmed under a fluorescent stereoscope.

Immunohistochemistry analysis

Brain tissue was collected and fixed in 4% paraformaldehyde solution overnight. Coronal sections (50 μm) were processed with the Vibratome instrument (VT1000S, Leica) and blocked 0.2% Triton X-100 and 10% goat serum solution for 1 h at room temperature. Sections were incubated overnight at 4°C with primary antibodies, followed by incubation with fluorophore-conjugated secondary antibodies and DAPI

for 1 h at room temperature. Slides were mounted using FluorSave reagent and imaged with a Leica TCS SP8 confocal microscope.

Immunoblotting

Whole-cell protein samples were prepared in RIPA buffer (25 mM Tris-HCl. pH7.6, 150 mM NaCl, 1% NP-40, 1% Sodium Deoxycholate, 0.1% SDS) containing 1× protease inhibitor cocktail (Thermo, 78439) and in some cases, supplemented with 1 mM PMSF and 1 mM NaF. Protein lysates were separated on pre-cast Bolt 4–12% Bis-Tris Plus Gels (Invitrogen, NW04127BOX) or Novex 10-20% Tricine Gels (Invitrogen, EC6625BOX) and transferred to nitrocellulose membranes. Membranes were subsequently probed using the relevant primary and secondary antibodies and relative protein levels were determined using the Odyssey Fc Imager (LI-COR).

Quantitative PCR

Total RNA was extracted from cells using the RNeasy kit (Qiagen) according to the manufacturer's protocol. RNA was used to generate cDNA by reverse transcriptase PCR using the High Capacity cDNA Reverse Transcription Kit (Applied Biosystems). Relative mRNA expression levels were determine using SYBR Green I detection chemistry (Applied Biosystems) on the QuantStudio instrument. To examine human *INK4A* mRNA levels we used the following primers (For 5'-GAAGGTCCCTCAGACATCCCC-3' and Rev 5'-CCCTGTAGGACCTTCGGTGAC-3'. The housekeeping gene *GAPDH* (For 5'-GGAGCGAGATCCCTCCAAAAT-3' and Rev 5'-GGCTGTTGTCATACTTCTCATGG-3') was used as a control normalization.

For absolute quantifications, two plasmid DNA samples, containing either the endogenous *H3F3A* sequence or codon-optimized exogenous H3.3-encoding sequence, had their concentrations measured using a Nanodrop ND-1000 spectrophotometer. Primers were designed and confirmed to highly specifically amplify the endogenous *H3F3A* sequence (For 5'-TGTGGCGCTCCGTGAAATTAG-3' and Rev 5'-CTGCAAAGCACCGATAGCTG-3') or the codon-optimized transgene sequence (For 5'-CTTGCGGTTCCAGAGTGCC-3' and Rev 5'-CCTAATGCGCCGAGCCAG-3'). Dilution series of the two plasmid samples were performed to generate standard curves using SYBR Green I detection chemistry (NEB) on a QuantStudio 3 Real-Time PCR System (Applied Biosystems). These

standard curves were used to estimate the copy numbers and relative levels of endogenous/exogenous H3.3 transcripts from each cell line.

RNA sequencing

Total RNA was isolated from cells using the RNeasy Mini Kit (Qiagen, 74106) in accordance with the manufacturer's instructions. The quality of extracted RNA was confirmed using the TapeStation (Agilent) with the RNA ScreenTape assay reagents (Agilent, 5067-5576). One µg of total RNA was used/sample as library prep input. Libraries were generated using the NEBNext Ultra RNA Library Prep kit for Illumina (NEB, E7530L) in accordance with the manufacturer's instructions. Library DNA was quantified using the Qubit, and size distributions were ascertained on a Tapestation (Agilent) using the D1000 ScreenTape assay reagents (Agilent, 5067–5583). This information was used to calculate pooling ratios for multiplex library sequencing. Pooled libraries were diluted and processed for 75 bp single-end sequencing on an Illumina NextSeq instrument using the NextSeq 500 High Output v2 kit (75 cycle) (Illumina, FC-404–2005) in accordance with the manufacturer's instructions.

Quant-seq

Total RNA was isolated following 24 h of control (DMSO) or Tazemetostat (2 µM) treatment of DIPGXIII cell cultures. The quality of extracted RNA was confirmed using the TapeStation (Agilent) with the RNA ScreenTape assay reagents (Agilent, 5067-5576). 500 ng of total RNA was used/sample as library prep input. Libraries were generated using the QuantSeq 3' mRNA-seq Library Prep Kit FWD for Illumina (Lexogen, 015.24) in accordance with the manufacturer's instructions. Library DNA was quantified using the Qubit, and size distributions were ascertained on a Tapestation (Agilent) using the D1000 ScreenTape assay reagents (Agilent, 5067–5583). This information was used to calculate pooling ratios for multiplex library sequencing. Pooled libraries were diluted and processed for 75 bp single-end sequencing on an Illumina NextSeq instrument using the NextSeq 500 High Output v2 kit (75 cycle) (Illumina, FC-404–2005) in accordance with the manufacturer's instructions. The Lexogen Bluebee Quantseq DE pipeline (v1.4.0) was utilized to quantify gene expression levels and differentially expressed genes using default parameters.

Quantitative Chromatin Immunoprecipitation (ChIP)

Cells were fixed in culture media containing 1% formaldehyde at room temperature for 10 min. Formaldehyde was quenched with glycine at 0.125 M, followed by a 5 min incubation at room temperature. Fixed cells were washed twice with 4ºC PBS. Nuclei were extracted with LB1 buffer (50 mM HEPES, 140 mM NaCl, 1 mM EDTA, 10% Glycerol, 0.5% NP40, 0.25% Triton X-100) containing 1× protease inhibitor cocktail (Thermo, 78439). Cells were pelleted by and resuspended in LB2 buffer (10 mM Tris ph8.0, 200 mM NaCl, 1 mM EDTA, 0.5 mM EGTA) containing 1× protease inhibitor cocktail. Extracted nuclei were lysed using ChIP sonication buffer (50 mM HEPES, 140 mM NaCl, 1 mM EDTA, 1 mM EGTA, 1% Triton X-100, 0.1% Sodium Deoxycholate, 0.3% SDS) containing 1× protein inhibitor cocktail. For quantitative ChIP analyses (ChIP-Rx) spike-in chromatin was prepared from mESCs and added to human NSC samples (1:10 ratio, cell number) at this point in the preparation procedure.

Chromatin samples were sheared using a Soniprep 150 for 5 min total sonication time, at 50% power and a duty cycle of 1 sec on/4 sec off. The SDS concentration of the sheared samples was reduced to 0.1% by diluting with ChIP buffer without SDS. ChIPs were performed O/N at 4ºC. For details on antibodies used please see below. Following O/N incubation 50 µl of Protein G Dynal beads were added to each sample and incubated for 2 h at 4ºC. Beads were washed 2× with ChIP reaction buffer (50 mM HEPES, 140 mM NaCl, 1 mM EDTA, 1 mM EGTA, 1% Triton X-100, 0.1% Sodium Deoxycholate, 0.1% SDS), 1× with High Salt Buffer (50 mM HEPES, 500 mM NaCl, 1 mM EDTA, 1 mM EGTA, 1% Triton X-100, 0.1% Sodium Deoxycholate, 0.1% SDS), 1× with LiCl Detergent Wash Buffer (20 mM Tris-HCl pH8.0, 1 mM EDTA, 250 mM LiCl, 0.5% NP40, 0.5% Sodium Deoxycholate), 1× with TE containing 50 mM NaCl. Samples were eluted for 60 min at 65ºC using ChIP Elution Buffer (50 mM Tris-HCl pH8.0, 10 mM EDTA, 1% SDS). Following an overnight reversal of crosslinks at 65ºC, enriched DNA fragments were purified using Qiagen MinElute PCR purification kit (Qiagen, 28006).

ChIP library preparation

ChIP purified DNA was quantified using a Qubit fluorimeter (Invitrogen), and 2–40 ng of DNA/ChIP was used to generate ChIP-seq libraries with the ThruPLEX DNA-seq kit

(Rubicon Genomics, R400427). Library DNA was quantified using the Qubit, and size distributions were ascertained on a Tapestation (Agilent) using the D1000 ScreenTape assay reagents (Agilent, 5067–5583). This information was used to calculate pooling ratios for multiplex library sequencing. Pooled libraries were diluted and processed for either 75 bp single-end or 36 bp paired-end sequencing on an Illumina NextSeq instrument using the NextSeq 500 High Output v2 kit (75 cycle) (Illumina, FC-404–2005) in accordance with the manufacturer's instructions.

Antibodies

Anti-SUZ12 (Cell Signaling, 3737S, Lot. 6) monoclonal rabbit antibody used in ChIP at a dilution of 1/50. Anti-H3K4me3 (Thermo Scientific, PA5-40086) used antibody used in ChIP at 5 µg/ChIP. Anti-H3K4me1 (Cell Signaling, 5326S, Lot. 1) monoclonal rabbit antibody used in ChIP at a dilution of 1/50. Anti-H3K27me1 (Active Motif, 61015, Lot. 32115011) monoclonal mouse antibody used in immunoblot at 1/2,500. Anti-H3K27me2 (Cell Signaling, 9728S, Lot. 15) monoclonal rabbit antibody used in ChIP at a dilution of 1/62.5 and immunoblot at 1/2,000. Anti-H3K27me3 (Cell Signaling, C36B1, custom lot) monoclonal rabbit antibody used in ChIP at 5 µg/ChIP and immunoblot at 1/1,000. Anti-H3K27ac (Abcam, ab4729, Lot. GR150367-2) polyclonal rabbit antibody used in ChIP at 5 µg/ChIP and immunoblot at 1/2,000. Anti-V5 (Thermo Scientific, R96025, Lot. 1923773) mouse monoclonal antibody used in ChIP at 5 µg/ChIP and immunoblot at 1/2000. Anti-BMI1 (Cell Signaling, 6964S, Lot. 1) monoclonal rabbit antibody used in ChIP at a dilution of 1/50. Anti-Histone H3.3 (Millipore, 09-838, Lot. 3310680) polyclonal rabbit antibody used in immunoblot at a dilution of 1/1,000. Anti-βActin (Proteintech, 60008-1-Ig) monoclonal mouse antibody used in immunoblot at a dilution of 1/5,000. Anti-Histone H3 (Active Motif, 39763, Lot. 28313014) monoclonal mouse antibody used in immunoblot at a dilution of 1/5,000. Anti-p16 (Santa Cruz, sc-56330, Lot. E2313) monoclonal mouse antibody used in immunoblot at a dilution of 1/200. Anti-H3K27M (Abcam, ab190631, Lot. GR239194-15) monoclonal rabbit antibody used in immunoblot at a dilution of 1/1,000. Mouse anti-V5-tag (eBioscience #14679682) and rabbit anti-Ki67 antibodies were used for the histological analysis at a 1:1,000 dilution. Secondary antibodies for immunoblotting: Goat Anti-Mouse IgG (LI-COR, 925-32210, Lot. C80816-10) used at a dilution of 1/5,000; Goat Anti-Rabbit IgG (LI-COR, 925-68071, Lot. C71214-01) used

at a dilution of 1/5,000 and Goat Anti-Rabbit IgG (LI-COR, 927-32211, Lot. D00804-07) used at a dilution of 1/4,000.

ChIP-Rx data analysis

Chromosome names for the mouse genome were modified with the prefix 'mm10_' and a meta-genome was created by concatenating the human and mouse reference genomes (hg38 and mm10 respectively) prior to indexing with bowtie2 (v1.2.2)[49] as described[50]. Reads were aligned to the metagenome using Bowtie2 using default parameters with the exception of --no-unal. Non-unique read alignments were filtered out using Samtools (v1.7)[51] to exclude those with an alignment quality of less than 2 and the ''mm10_" prefix appended to chromosome names was used to separate reads as aligned to the reference human or spike-in mouse genomes. Samtools was used to convert SAM files to BAM files and to remove duplicate aligned reads. Spike-in normalization factors were calculated for each ChIP using the formula for normalized reference-adjusted RPM (RRPM) as described[50] (1/million spike-in reads). Bigwig files were generated using the bamCoverage tool from the deepTools suite (v3.3.0)[52] with a bin size of 10 and scaled using the RRPM normalization factor derived for each sample. Bam files were converted to BED format using the bamToBed function in BEDTools (v2.26.0)[53] and used for peak calling with HOMER (v4.10)[54], using BED files from input ChIP-Rx as a control. Sets of peaks for each of the 2 embryo samples were intersected and only those identified in both were retained for further analyses including generation of average plots using the computeMatrix and plotProfile functions in deepTools and tornado plots in EaSeq[55].

The hg38 reference genome was split into 1-kb and 10-kb windows using the makewindows function in BEDTools and regions in a custom blacklist file (based on the DAC ENCODE blacklist) removed using bedtools intersect with the -v and -wa flags. BEDTools coverage was used to summarize overlapping read alignments in BAM files within these bins and scaled using RRPM normalization. Resulting counts were used for the generation of chromosome wide coverage line graphs and XY density scatter plots. BEDTools complement was used to retrieve regions of the genome which did not contain an annotated SUZ12 peak and 1-kb bins from these regions were used for calculating the degree of loss/gain of SUZ12 and H3K27me3 within and outside SUZ12 peak regions after subtracting background levels of SUZ12

and H3K27me3 calculated by levels of these marks in H3K27ac peak regions per 1 kb.

Promoter regions were identified by taking -1,000 bases upstream and +100 bases downstream of annotated transcription start sites in the Ensembl 98 hg38 genome annotation. Active promoters were defined by overlapping H3K27ac peak sets with gene promoter regions defined within the hg38 build of the human genome. Only promoters overlapping H3K27ac-enriched regions in both biological replicate NSC lines were retained for further analysis. Active enhancers were identified with H3K27ac ChIP-Rx datasets analyzed using ROSE[56,57]. Only enhancer regions that were identified in both biological replicates were retained for further analysis. PRC2 target promoters were defined by overlapping SUZ12 peak sets with gene promoter regions defined within the hg38 build of the human genome. Only promoters overlapping SUZ12-bound regions in both biological replicate NSC lines were retained for further analysis. H3K27ac was quantified at these promoter and enhancer peak region sets using BEDTools coverage and counts normalized for RRPM and peak size. Enhancers were assigned to their nearest protein coding gene using BEDTools closest for integration with RNA-seq data.

RNA sequencing data analysis

RNA-seq reads were aligned to the human reference genome (hg38) using the hisat2 algorithm (v2.1.0)[58] and SAM files converted to sorted BAM using Samtools (v1.7)[32,58]. Read alignments were assigned to gene identifier features annotated in the Ensembl 98 hg38 genome annotation using featureCounts (v1.6.4)[59]. The DESeq2 R package (v1.24.0)[60] was utilized to identify genes differentially expressed genes at a >1.5 fold change with a >20 baseMean expression and a < 0.05 Benjamini-Hochberg adjusted *P* value.

Omni-ATAC-seq

Omni-ATAC-seq was conducted as previously described[37]. Briefly, wild-type or K27M-mutant H3.3 NSC cultures were treated with DNase at 200U/ml for 30 min at 37ºC prior to harvesting. Cells were then harvested, and 50,000 viable cells resuspended in 50 µl ATAC-Resuspension Buffer (RSB) (10 mM Tris-HCl pH 7.4, 10 mM NaCl, 3

mM $MgCl_2$) containing 0.1% Tween-20, 0.1% NP40 and 0.01% Digitonin. Following a 3 min incubation at 4ºC, cells were washed with 1 ml of ATAC-RSB with 0.1% Tween. Samples were then centrifuged to collect extracted nuclei and resuspended in a 50 µl transposition mixture (25 µl 2× TD buffer, 2.5 µl transposase (100 nM final), 16.5 µl PBS, 0.5 µl 1% digitonin, 0.5 µl 10% Tween-20, 5 µl H_2O). Transposition reactions were incubated for 30 min at 37ºC.

Transposed DNA fragments were purified using Qiagen MinElute columns and eluted samples used directly for PCR amplification to append Illumina adapters and index sequences. PCR amplified library material was purified using AMPure beads, quantified using the Qubit and size distributions ascertained on a Tapestation (Agilent) using the D1000 ScreenTape assay reagents (Agilent, 5067–5583). Pooled libraries were diluted and processed for 36 bp paired-end sequencing on an Illumina NextSeq instrument using the NextSeq 500 High Output v2 kit (75 cycle) (Illumina, FC-404–2005) in accordance with the manufacturer's instructions.

ATAC-seq data analysis

ATAC-seq reads were processed using *Trim galore* to remove standard Illumina adapters prior to alignment with *Bowtie2* in --paired --very-sensitive mode and with a maximum insert size of -X 1000. SAM files were processed into sorted, indexed BAM files using *Samtools* and quality statistics produced using *FastQC* and *MultiQC*[61]. A version of previously described ATAC-seq pipeline[62], was modified to handle 4 replicates and used to remove mitochondrial reads, correct read pairs, down sample to an even sequencing complexity, mark duplicates with *Picard*, call peaks with *macs2*, filter blacklisted sites, and identify differentially accessible chromatin in macs2 peak only mode using csaw[63] with loess-normalization.

Gene ontology analysis

Gene ontology analysis was carried out on differentially expressed and non-differentially expressed genes as well as on promoter regions associate with genes differentially bound by SUZ12 using ShinyGo (v0.60)[64] with genes annotated with GO terms present in Ensembl BioMart V96. GO terms enriched with an adjusted *P* value below 0.05 were considered significant.

Data Availability

All sequencing datasets generated during this work have been deposited in the Gene Expression Omnibus under accession number GSE154267.

Methods References:

46. Conti, L. *et al.* Niche-independent symmetrical self-renewal of a mammalian tissue stem cell. *PLoS Biol* **3**, e283 (2005).
47. Bressan, R.B. *et al.* Efficient CRISPR/Cas9-assisted gene targeting enables rapid and precise genetic manipulation of mammalian neural stem cells. *Development* **144**, 635-648 (2017).
48. Pollard, S.M. *et al.* Glioma stem cell lines expanded in adherent culture have tumor-specific phenotypes and are suitable for chemical and genetic screens. *Cell Stem Cell* **4**, 568-80 (2009).
49. Langmead, B. & Salzberg, S.L. Fast gapped-read alignment with Bowtie 2. *Nat Methods* **9**, 357-9 (2012).
50. Orlando, D.A. *et al.* Quantitative ChIP-Seq normalization reveals global modulation of the epigenome. *Cell Rep* **9**, 1163-70 (2014).
51. Li, H. *et al.* The Sequence Alignment/Map format and SAMtools. *Bioinformatics* **25**, 2078-9 (2009).
52. Ramirez, F. *et al.* deepTools2: a next generation web server for deep-sequencing data analysis. *Nucleic Acids Res* **44**, W160-5 (2016).
53. Quinlan, A.R. & Hall, I.M. BEDTools: a flexible suite of utilities for comparing genomic features. *Bioinformatics* **26**, 841-2 (2010).
54. Heinz, S. *et al.* Simple combinations of lineage-determining transcription factors prime cis-regulatory elements required for macrophage and B cell identities. *Mol Cell* **38**, 576-89 (2010).
55. Lerdrup, M., Johansen, J.V., Agrawal-Singh, S. & Hansen, K. An interactive environment for agile analysis and visualization of ChIP-sequencing data. *Nat Struct Mol Biol* **23**, 349-57 (2016).
56. Whyte, W.A. *et al.* Master transcription factors and mediator establish super-enhancers at key cell identity genes. *Cell* **153**, 307-19 (2013).
57. Loven, J. *et al.* Selective inhibition of tumor oncogenes by disruption of super-enhancers. *Cell* **153**, 320-34 (2013).
58. Kim, D., Paggi, J.M., Park, C., Bennett, C. & Salzberg, S.L. Graph-based genome alignment and genotyping with HISAT2 and HISAT-genotype. *Nat Biotechnol* **37**, 907-915 (2019).
59. Liao, Y., Smyth, G.K. & Shi, W. featureCounts: an efficient general purpose program for assigning sequence reads to genomic features. *Bioinformatics* **30**, 923-30 (2014).
60. Love, M.I., Huber, W. & Anders, S. Moderated estimation of fold change and dispersion for RNA-seq data with DESeq2. *Genome Biol* **15**, 550 (2014).
61. Ewels, P., Magnusson, M., Lundin, S. & Kaller, M. MultiQC: summarize analysis results for multiple tools and samples in a single report. *Bioinformatics* **32**, 3047-8 (2016).

62. Reske, J.J., Wilson, M.R. & Chandler, R.L. ATAC-seq normalization method can significantly affect differential accessibility analysis and interpretation. *Epigenetics Chromatin* **13**, 22 (2020).
63. Lun, A.T. & Smyth, G.K. csaw: a Bioconductor package for differential binding analysis of ChIP-seq data using sliding windows. *Nucleic Acids Res* **44**, e45 (2016).
64. Ge, S.X., Jung, D. & Yao, R. ShinyGO: a graphical gene-set enrichment tool for animals and plants. *Bioinformatics* **36**, 2628-2629 (2020).

Figure 1

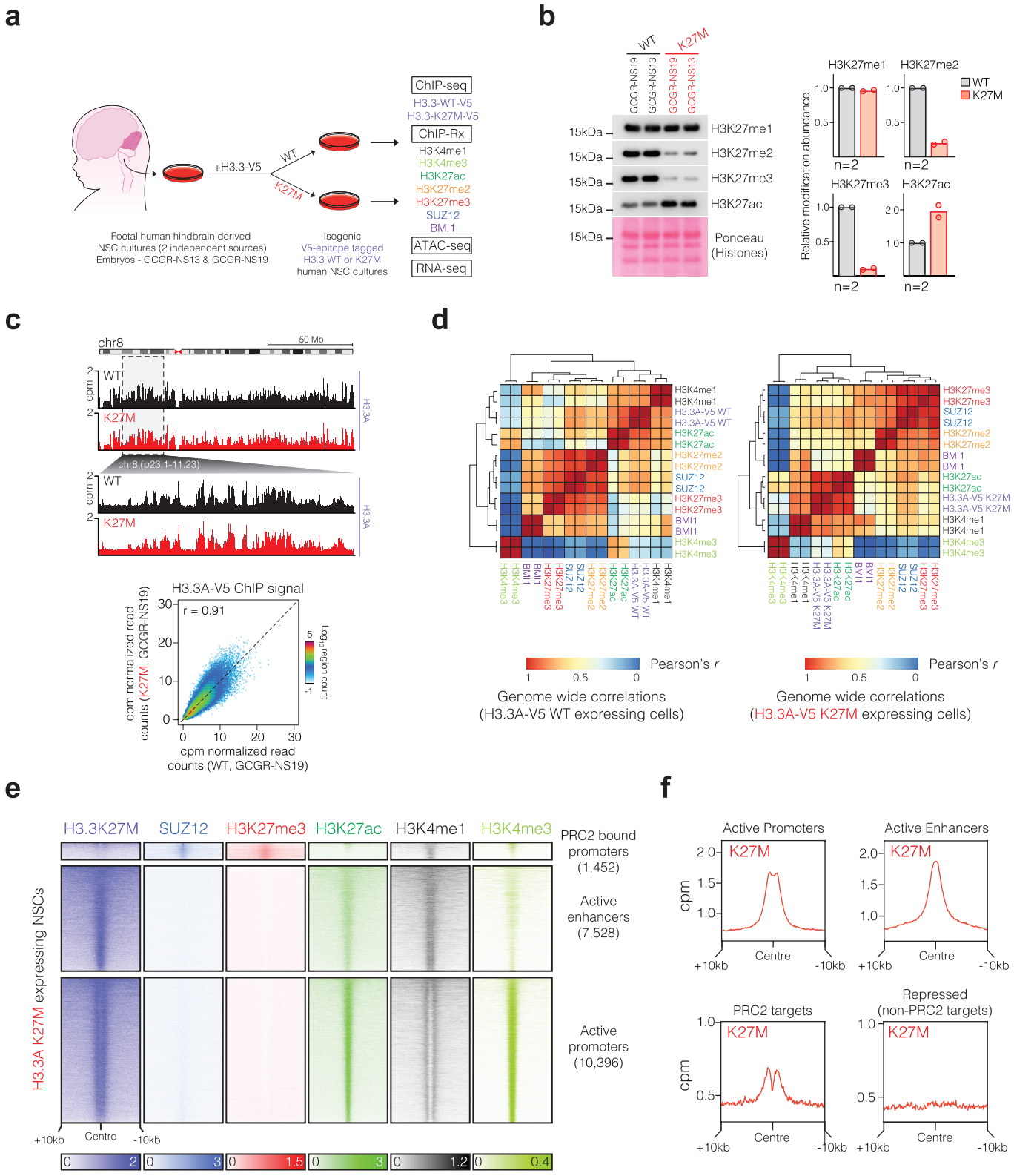
a
+H3.3-V5
WT
K27M
ChIP-seq
H3.3-WT-V5
H3.3-K27M-V5
ChIP-Rx
H3K4me1
H3K4me3
H3K27ac
H3K27me2
H3K27me3
SUZ12
BMI1
ATAC-seq
RNA-seq
Foetal human hindbrain derived
NSC cultures (2 independent sources)
Embryos - GCGR-NS13 & GCGR-NS19
Isogenic
V5-epitope tagged
H3.3 WT or K27M
human NSC cultures
b
WT
K27M
GCGR-NS19
GCGR-NS13
15kDa
H3K27me1
H3K27me2
H3K27me3
H3K27ac
Ponceau
(Histones)
Relative modification abundance
n=2
c
chr8
50 Mb
cpm
H3.3A
chr8 (p23.1-11.23)
H3.3A-V5 ChIP signal
r = 0.91
cpm normalized read counts (K27M, GCGR-NS19)
cpm normalized read counts (WT, GCGR-NS19)
d
Pearson's r
Genome wide correlations
(H3.3A-V5 WT expressing cells)
Genome wide correlations
(H3.3A-V5 K27M expressing cells)
e
H3.3K27M
SUZ12
H3K27me3
H3K27ac
H3K4me1
H3K4me3
H3.3A K27M expressing NSCs
PRC2 bound promoters (1,452)
Active enhancers (7,528)
Active promoters (10,396)
+10kb
Centre
-10kb
f
Active Promoters
Active Enhancers
PRC2 targets
Repressed (non-PRC2 targets)
K27M
cpm

Figure 2

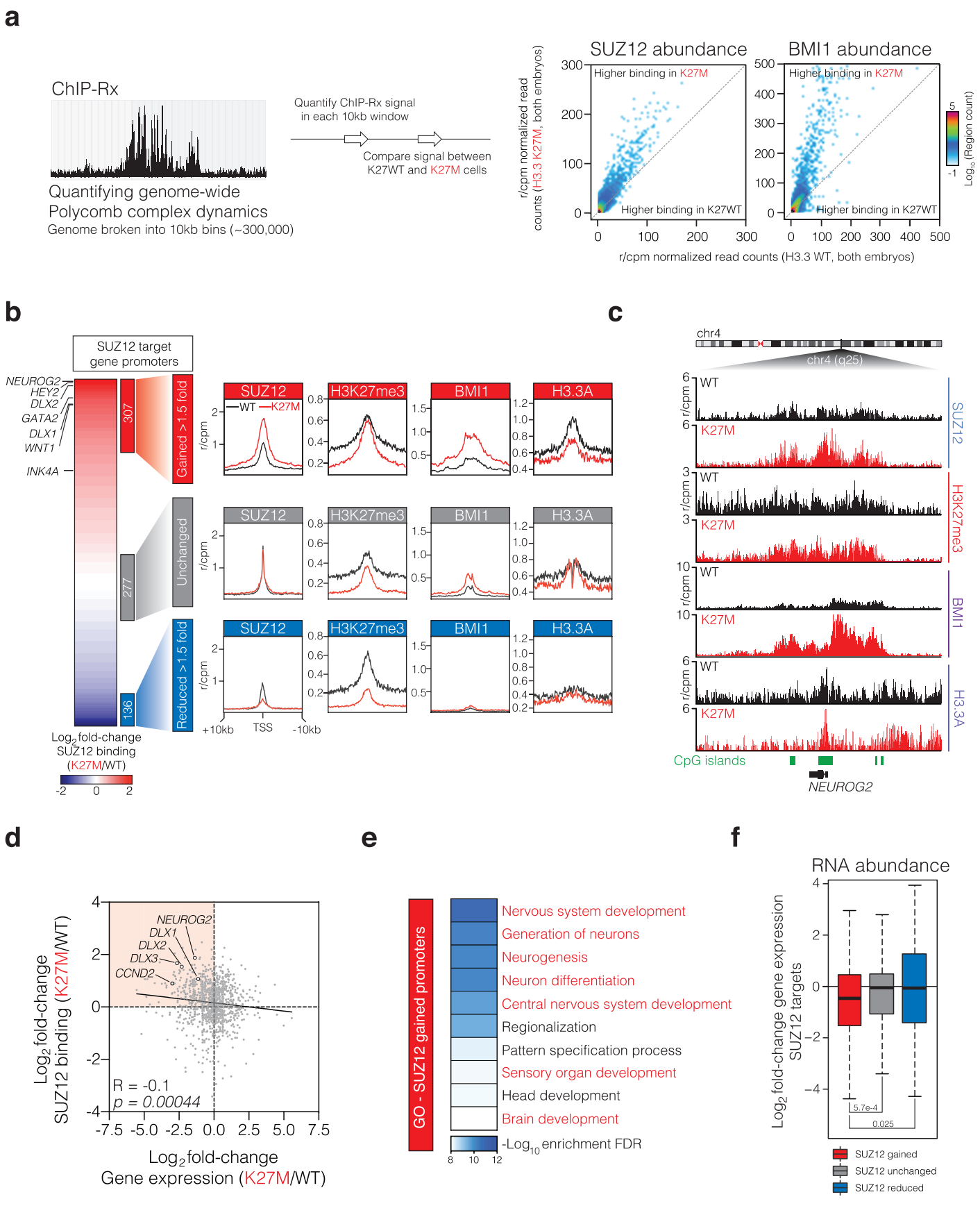
a
ChIP-Rx
Quantifying genome-wide
Polycomb complex dynamics
Genome broken into 10kb bins (~300,000)
Quantify ChIP-Rx signal
in each 10kb window
Compare signal between
K27WT and K27M cells
SUZ12 abundance
BMI1 abundance
Higher binding in K27M
Higher binding in K27WT
r/cpm normalized read
counts (H3.3 K27M, both embryos)
r/cpm normalized read counts (H3.3 WT, both embryos)
Log10 (Region count)
b
SUZ12 target
gene promoters
NEUROG2
HEY2
DLX2
GATA2
DLX1
WNT1
INK4A
307
277
136
Gained >1.5 fold
Unchanged
Reduced >1.5 fold
SUZ12
H3K27me3
BMI1
H3.3A
WT
K27M
r/cpm
+10kb
TSS
-10kb
Log2 fold-change
SUZ12 binding
(K27M/WT)
c
chr4
chr4 (q25)
CpG islands
NEUROG2
d
Log2 fold-change
SUZ12 binding (K27M/WT)
Log2 fold-change
Gene expression (K27M/WT)
NEUROG2
DLX1
DLX2
DLX3
CCND2
R = -0.1
p = 0.00044
e
GO - SUZ12 gained promoters
Nervous system development
Generation of neurons
Neurogenesis
Neuron differentiation
Central nervous system development
Regionalization
Pattern specification process
Sensory organ development
Head development
Brain development
-Log10 enrichment FDR
f
RNA abundance
Log2 fold-change gene expression
SUZ12 targets
5.7e-4
0.025
SUZ12 gained
SUZ12 unchanged
SUZ12 reduced

Figure 3

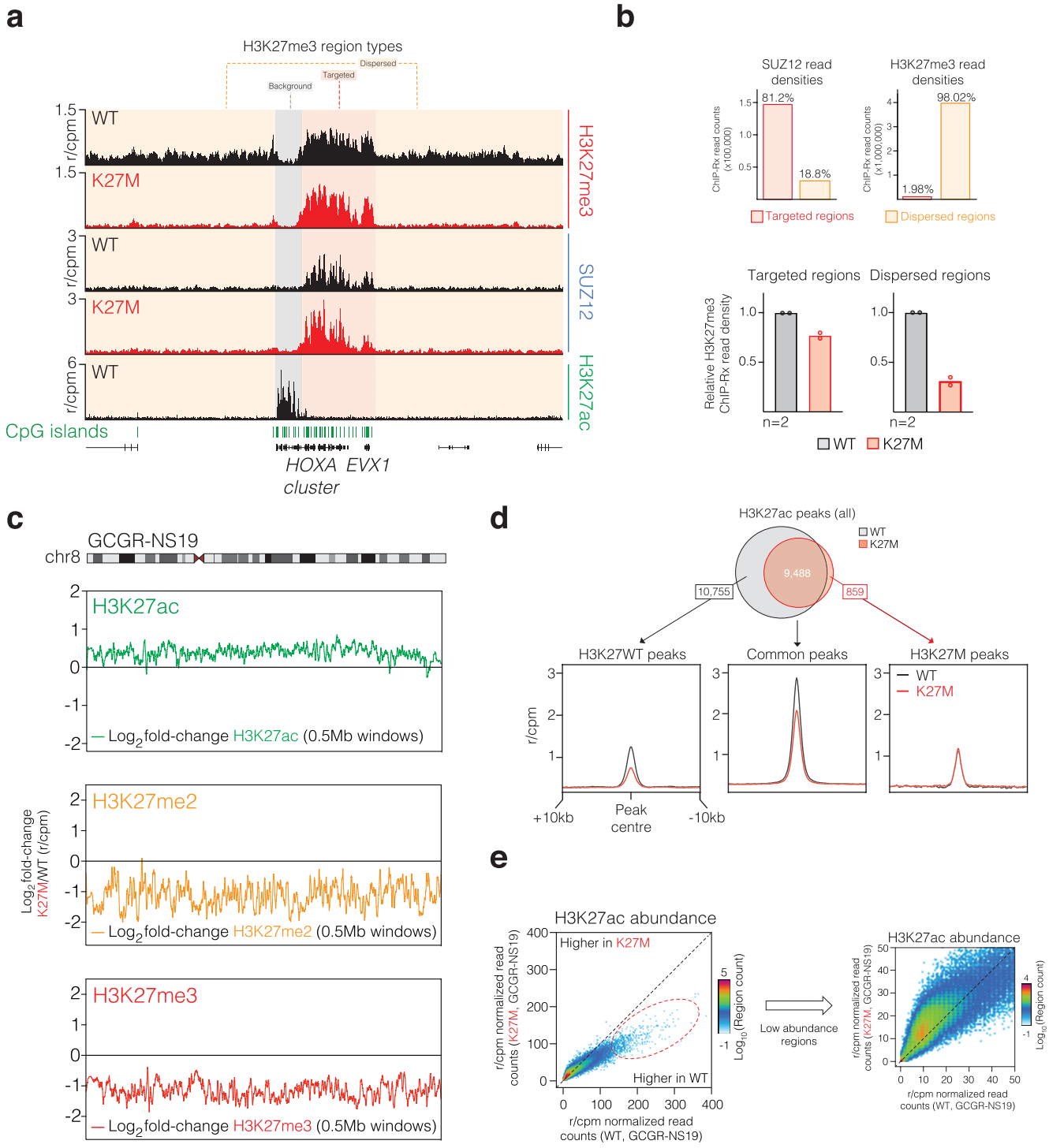
a
H3K27me3 region types
Dispersed
Targeted
Background
WT
K27M
r/cpm
H3K27me3
SUZ12
H3K27ac
CpG islands
HOXA EVX1 cluster
b
SUZ12 read densities
H3K27me3 read densities
81.2%
18.8%
1.98%
98.02%
ChIP-Rx read counts (x100,000)
ChIP-Rx read counts (x1,000,000)
Targeted regions
Dispersed regions
Relative H3K27me3 ChIP-Rx read density
n=2
WT
K27M
c
GCGR-NS19
chr8
H3K27ac
Log2 fold-change H3K27ac (0.5Mb windows)
H3K27me2
Log2 fold-change H3K27me2 (0.5Mb windows)
H3K27me3
Log2 fold-change H3K27me3 (0.5Mb windows)
Log2 fold-change K27M/WT (r/cpm)
d
H3K27ac peaks (all)
9,488
10,755
859
H3K27WT peaks
Common peaks
H3K27M peaks
+10kb
Peak centre
-10kb
e
H3K27ac abundance
Higher in K27M
Higher in WT
r/cpm normalized read counts (K27M, GCGR-NS19)
r/cpm normalized read counts (WT, GCGR-NS19)
Log10 (Region count)
Low abundance regions

Figure 4

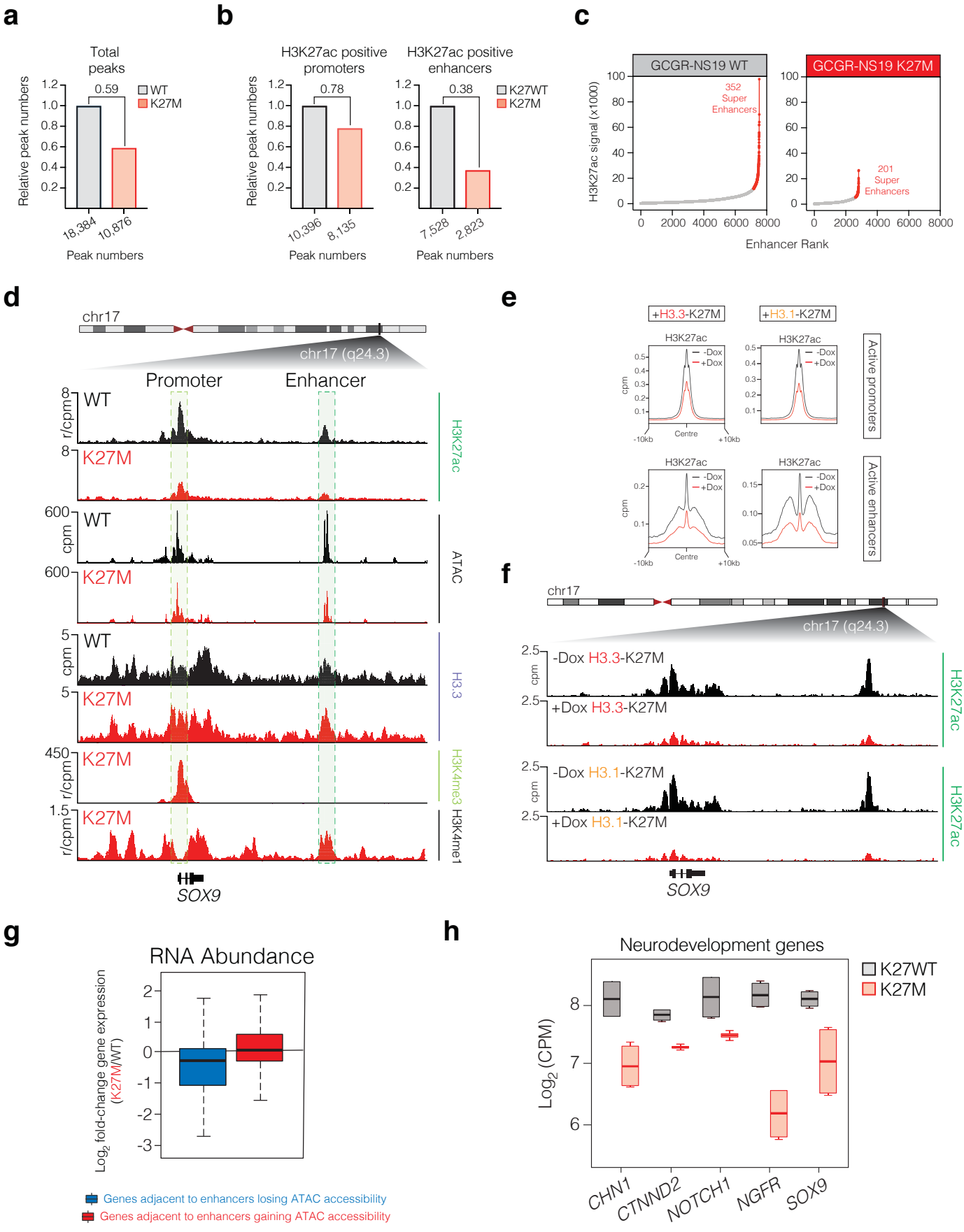
a
Total peaks
Relative peak numbers
0.59
WT
K27M
18,384
10,876
Peak numbers
b
H3K27ac positive promoters
H3K27ac positive enhancers
Relative peak numbers
0.78
0.38
K27WT
K27M
10,396
8,135
7,528
2,823
Peak numbers
c
GCGR-NS19 WT
GCGR-NS19 K27M
H3K27ac signal (x1000)
352 Super Enhancers
201 Super Enhancers
Enhancer Rank
d
chr17
chr17 (q24.3)
Promoter
Enhancer
WT
K27M
r/cpm
cpm
H3K27ac
ATAC
H3.3
H3K4me3
H3K4me1
SOX9
e
+H3.3-K27M
+H3.1-K27M
H3K27ac
-Dox
+Dox
cpm
Centre
-10kb
+10kb
Active promoters
Active enhancers
f
chr17
chr17 (q24.3)
-Dox H3.3-K27M
+Dox H3.3-K27M
-Dox H3.1-K27M
+Dox H3.1-K27M
cpm
H3K27ac
SOX9
g
RNA Abundance
Log2 fold-change gene expression (K27M/WT)
Genes adjacent to enhancers losing ATAC accessibility
Genes adjacent to enhancers gaining ATAC accessibility
h
Neurodevelopment genes
K27WT
K27M
Log2 (CPM)
CHN1
CTNND2
NOTCH1
NGFR
SOX9

Figure 5

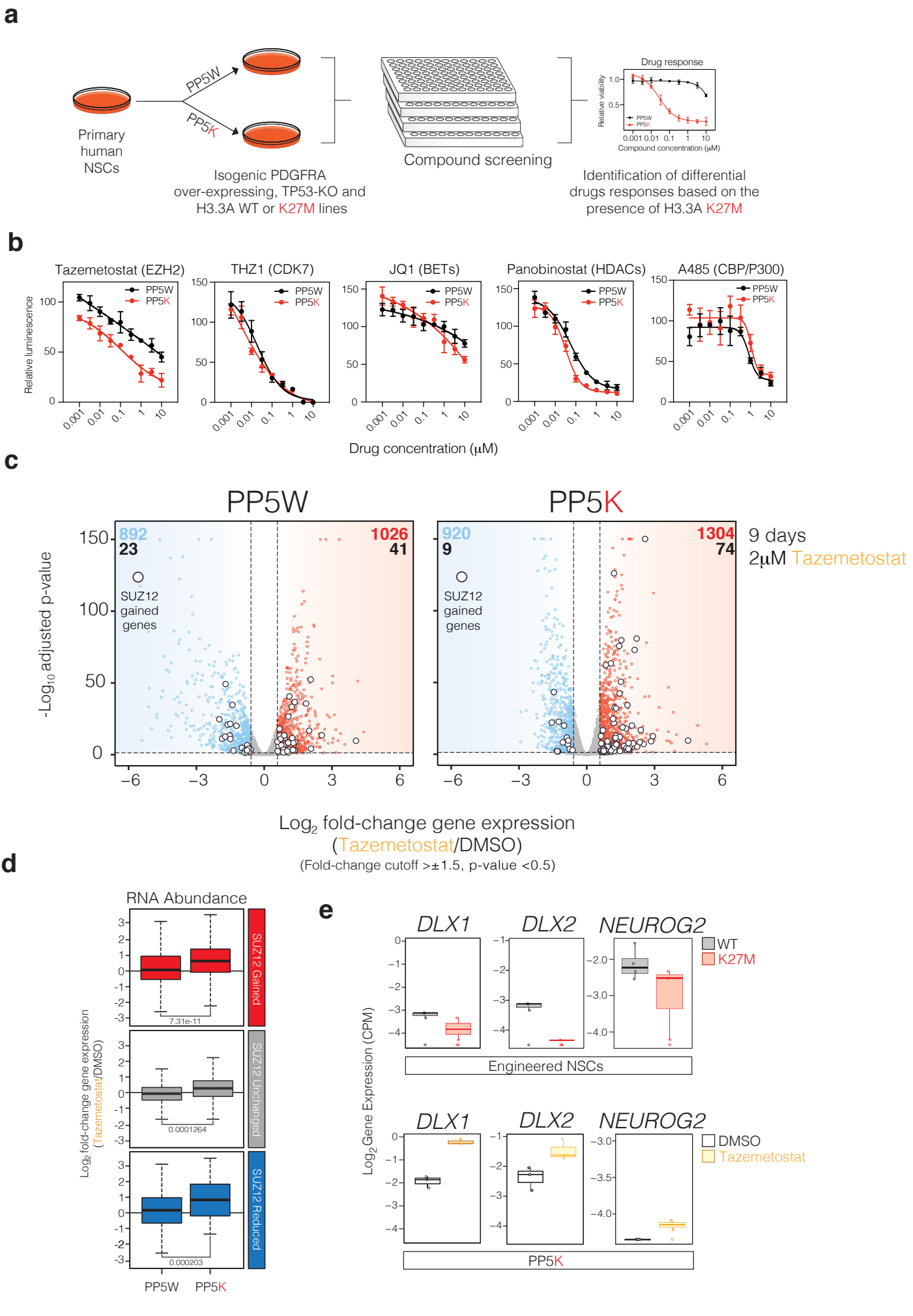
a
PP5W
PP5K
Primary human NSCs
Isogenic PDGFRA over-expressing, TP53-KO and H3.3A WT or K27M lines
Compound screening
Drug response
Relative viability
Compound concentration (μM)
Identification of differential drugs responses based on the presence of H3.3A K27M
b
Tazemetostat (EZH2)
THZ1 (CDK7)
JQ1 (BETs)
Panobinostat (HDACs)
A485 (CBP/P300)
Relative luminescence
Drug concentration (μM)
c
PP5W
PP5K
892
23
1026
41
920
9
1304
74
SUZ12 gained genes
-Log10 adjusted p-value
9 days
2μM Tazemetostat
Log2 fold-change gene expression
(Tazemetostat/DMSO)
(Fold-change cutoff >±1.5, p-value <0.5)
d
RNA Abundance
SUZ12 Gained
SUZ12 Unchanged
SUZ12 Reduced
7.31e-11
0.0001264
0.000203
Log2 fold-change gene expression (Tazemetostat/DMSO)
e
DLX1
DLX2
NEUROG2
WT
K27M
Engineered NSCs
Log2 Gene Expression (CPM)
DMSO
Tazemetostat
PP5K

Figure 6

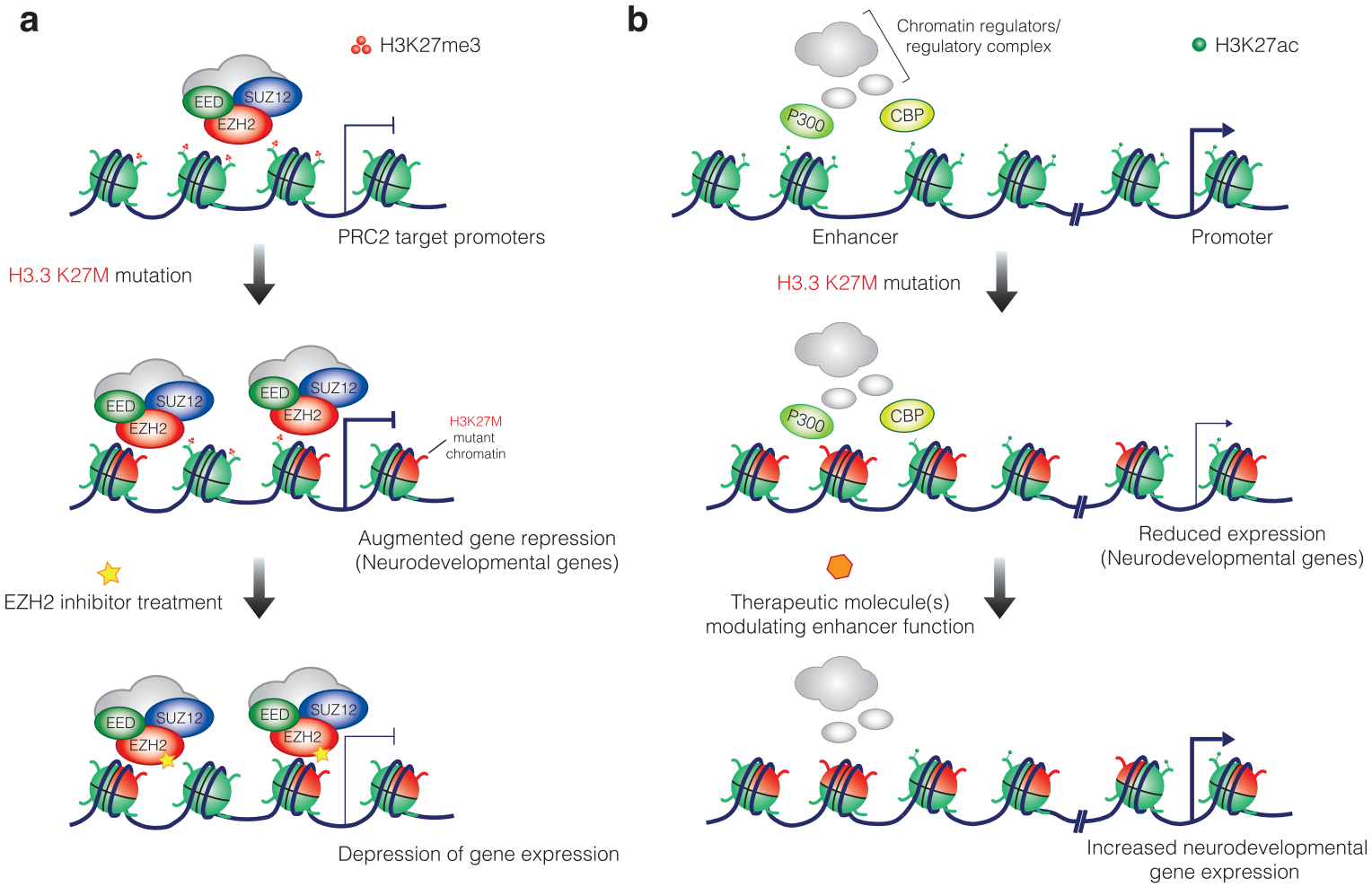
a
H3K27me3
EED
SUZ12
EZH2
PRC2 target promoters
H3.3 K27M mutation
H3K27M
mutant
chromatin
Augmented gene repression
(Neurodevelopmental genes)
EZH2 inhibitor treatment
Depression of gene expression
b
Chromatin regulators/
regulatory complex
H3K27ac
P300
CBP
Enhancer
Promoter
H3.3 K27M mutation
Reduced expression
(Neurodevelopmental genes)
Therapeutic molecule(s)
modulating enhancer function
Increased neurodevelopmental
gene expression

Extended Data Figure 1

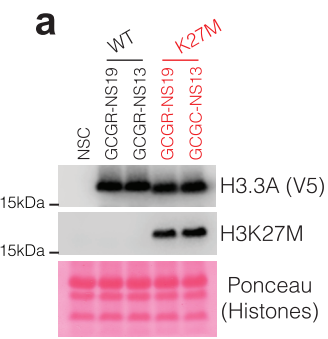

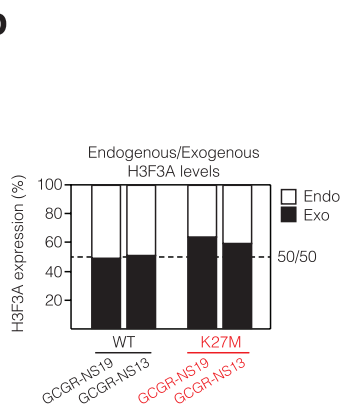

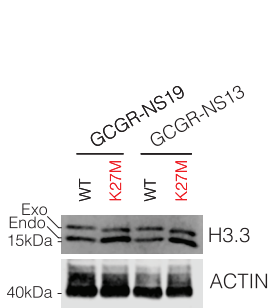

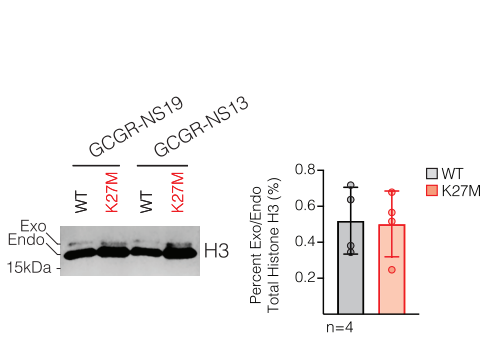

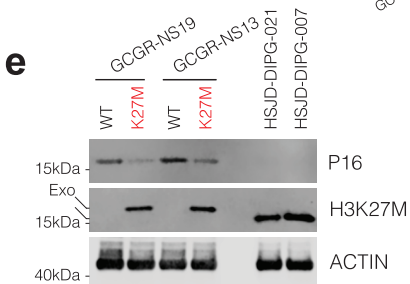

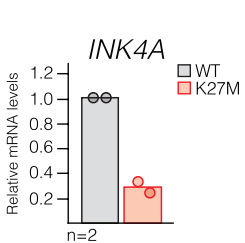

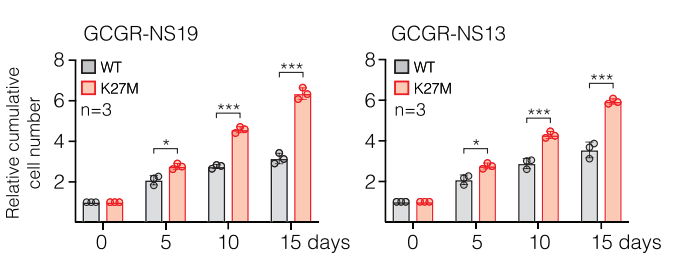

Extended Data Figure 2

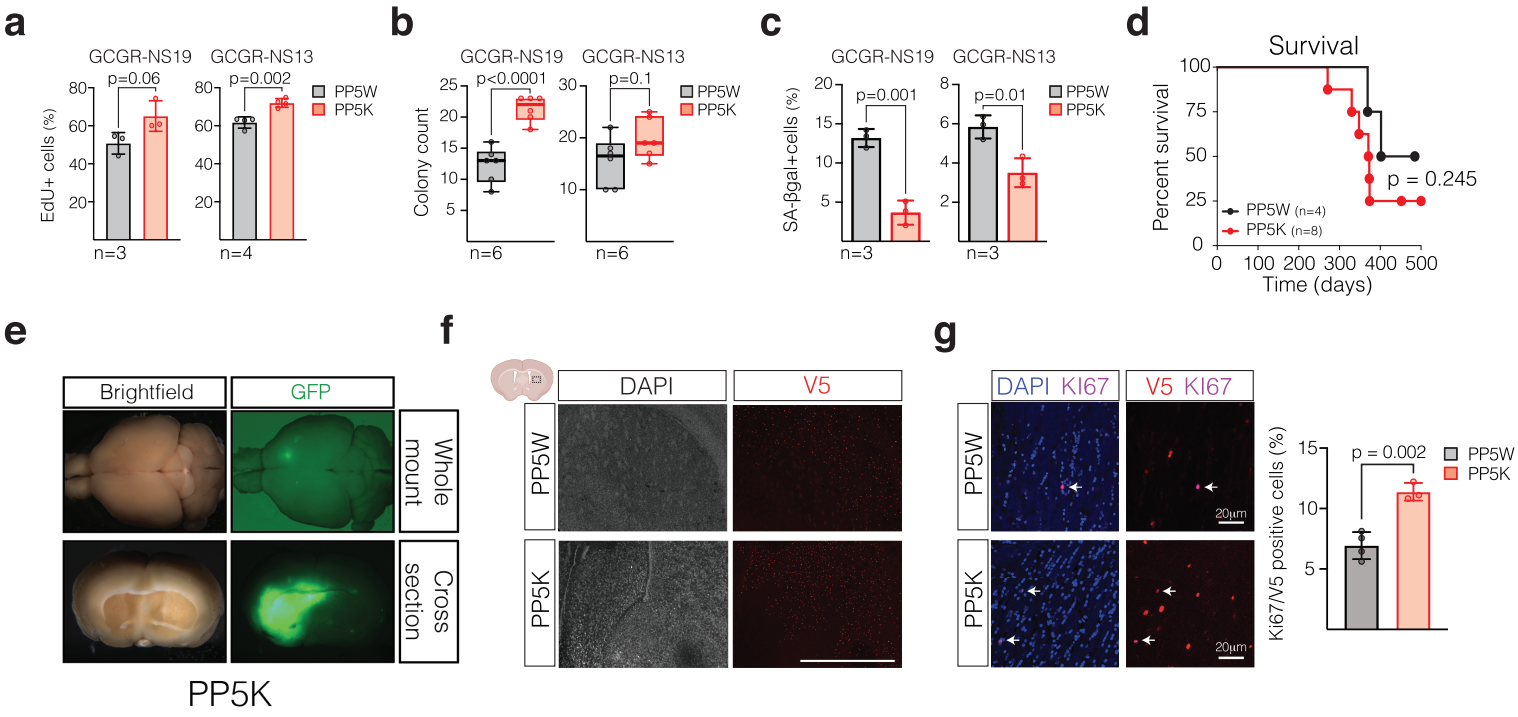

Extended Data Figure 3

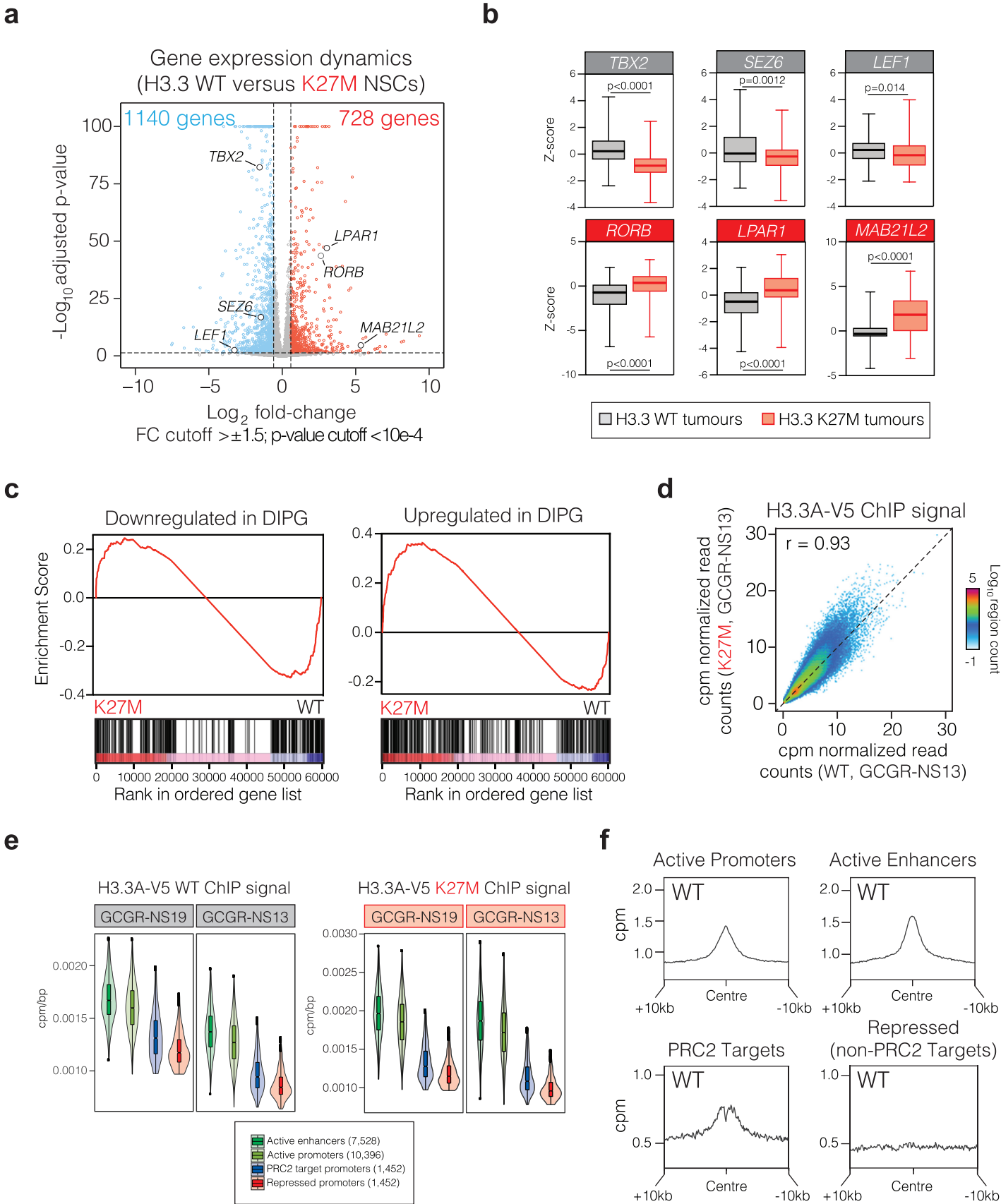

Extended Data Figure 4

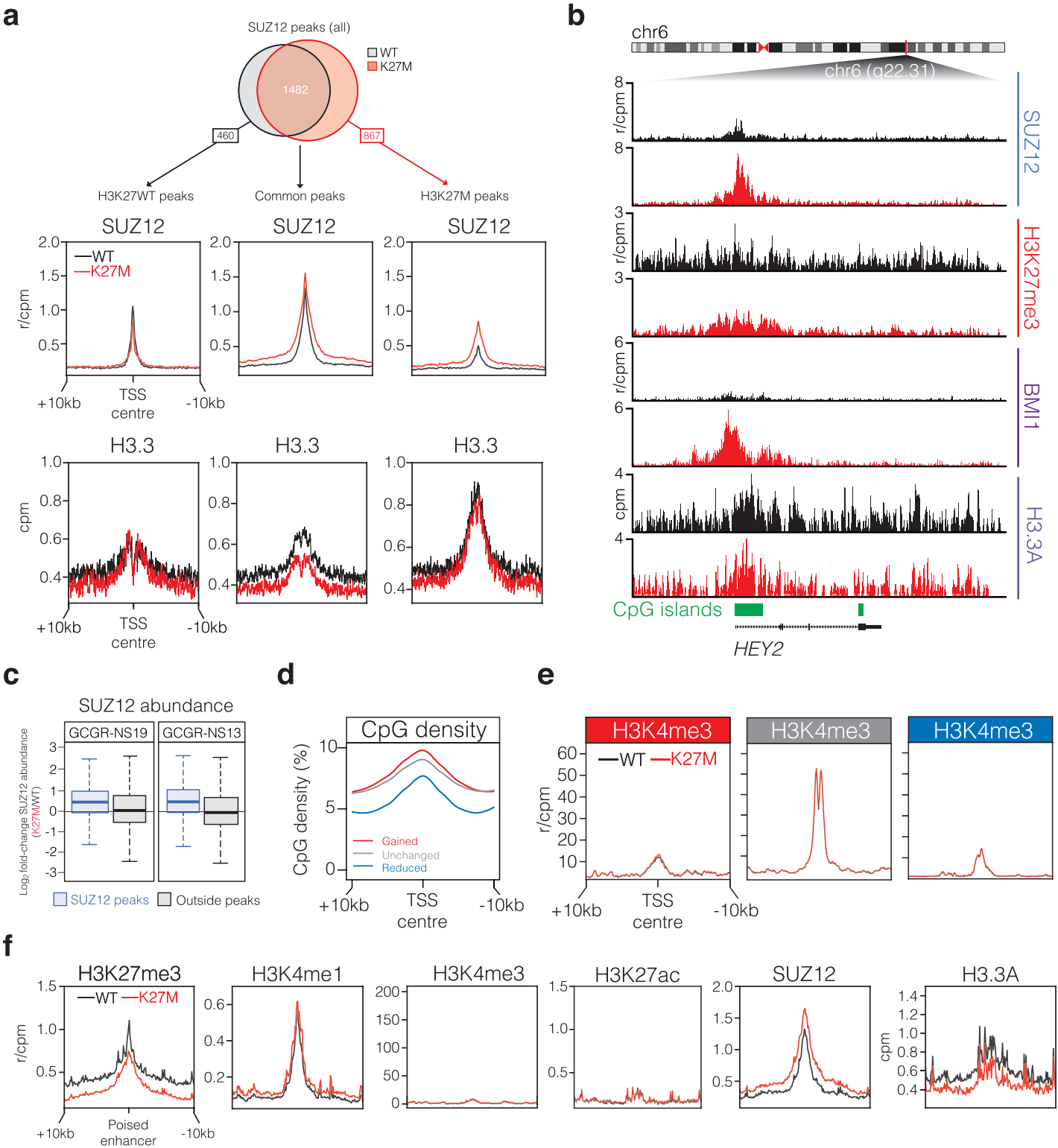

Extended Data Figure 5

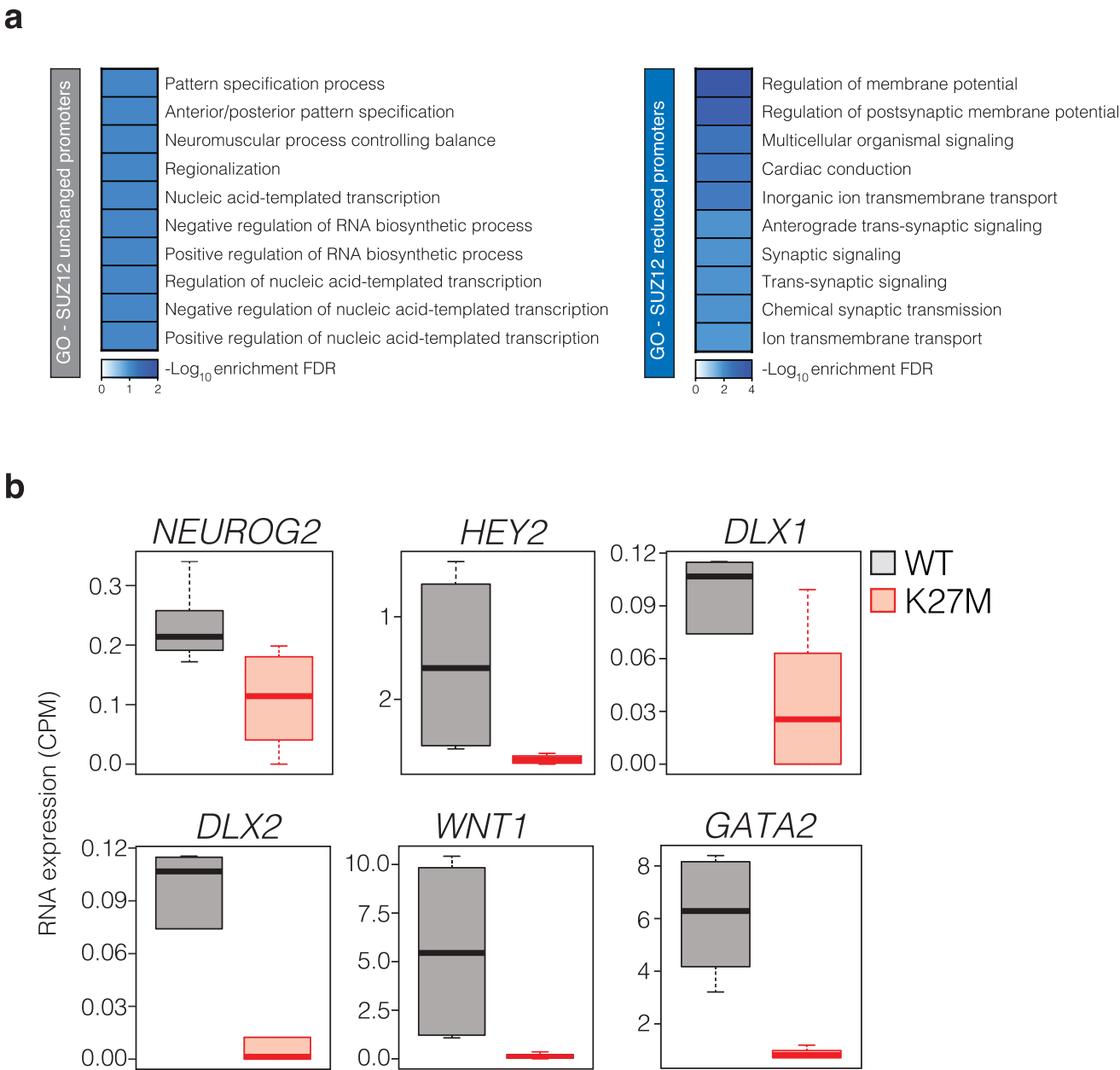

Extended Data Figure 6

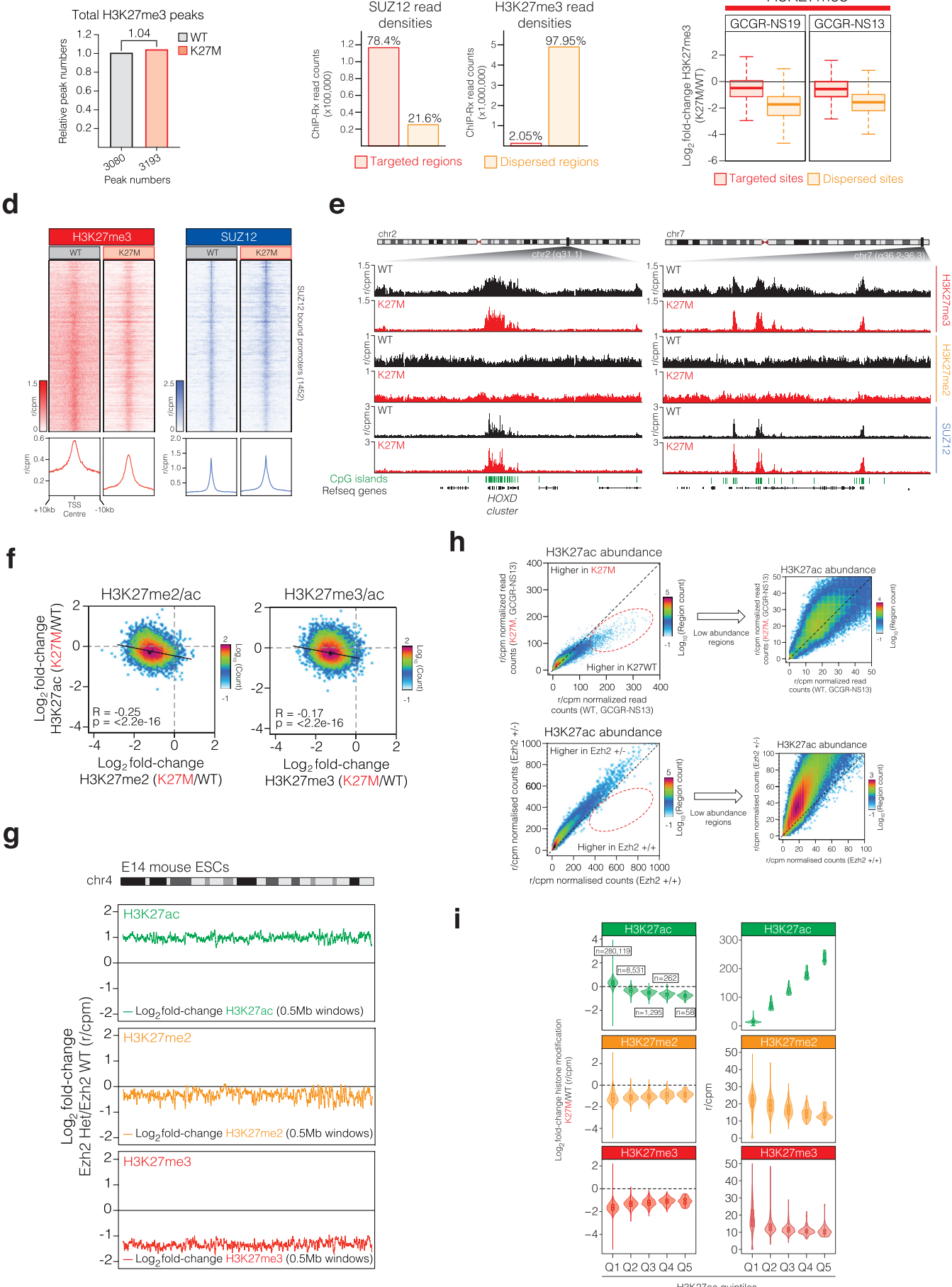

Extended Data Figure 7

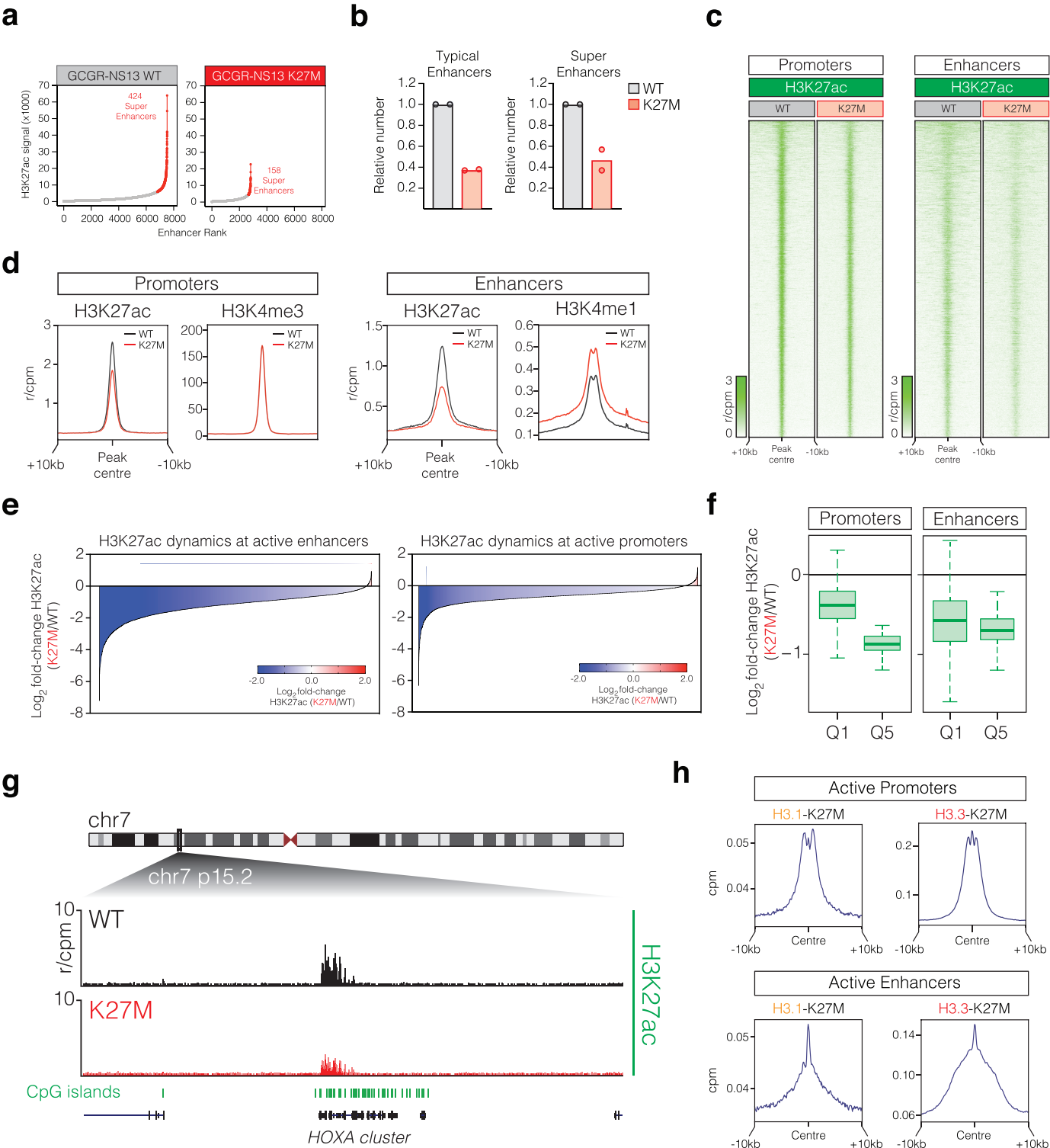

Extended Data Figure 8

a

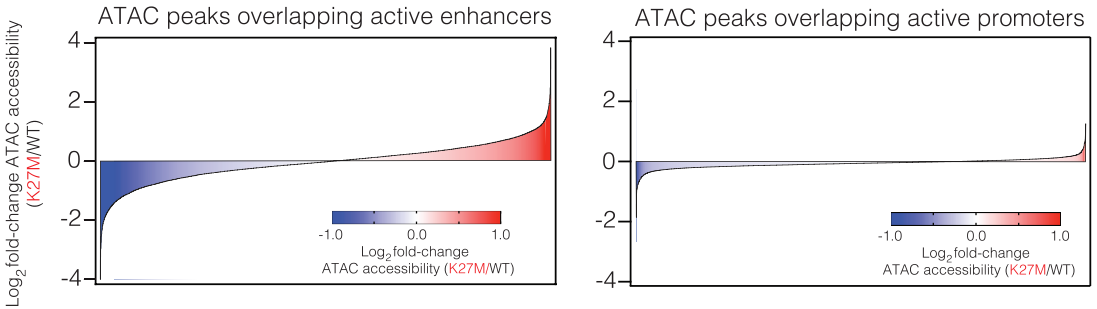

b

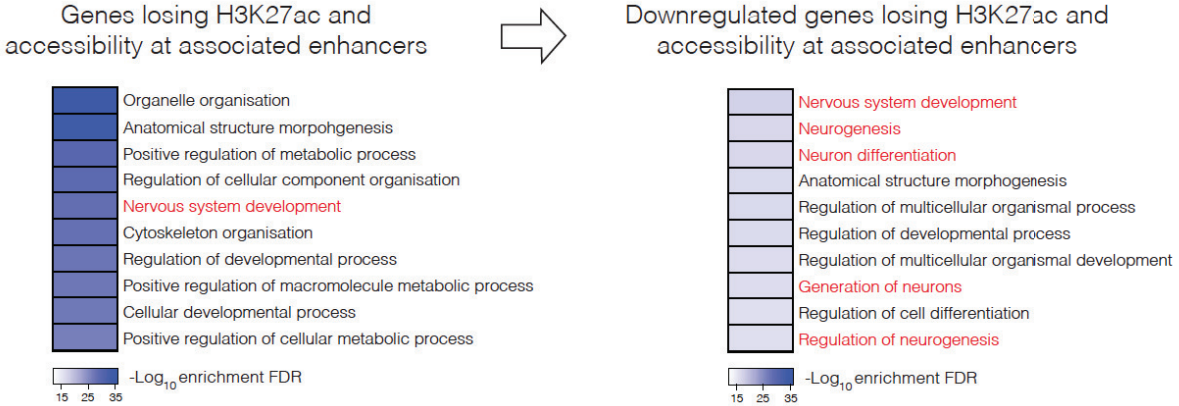

c

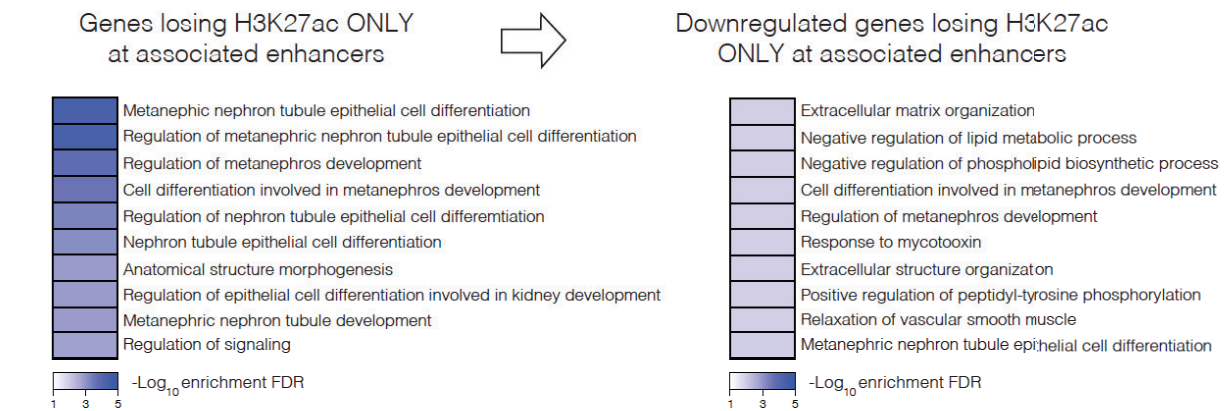

Extended Data Figure 9

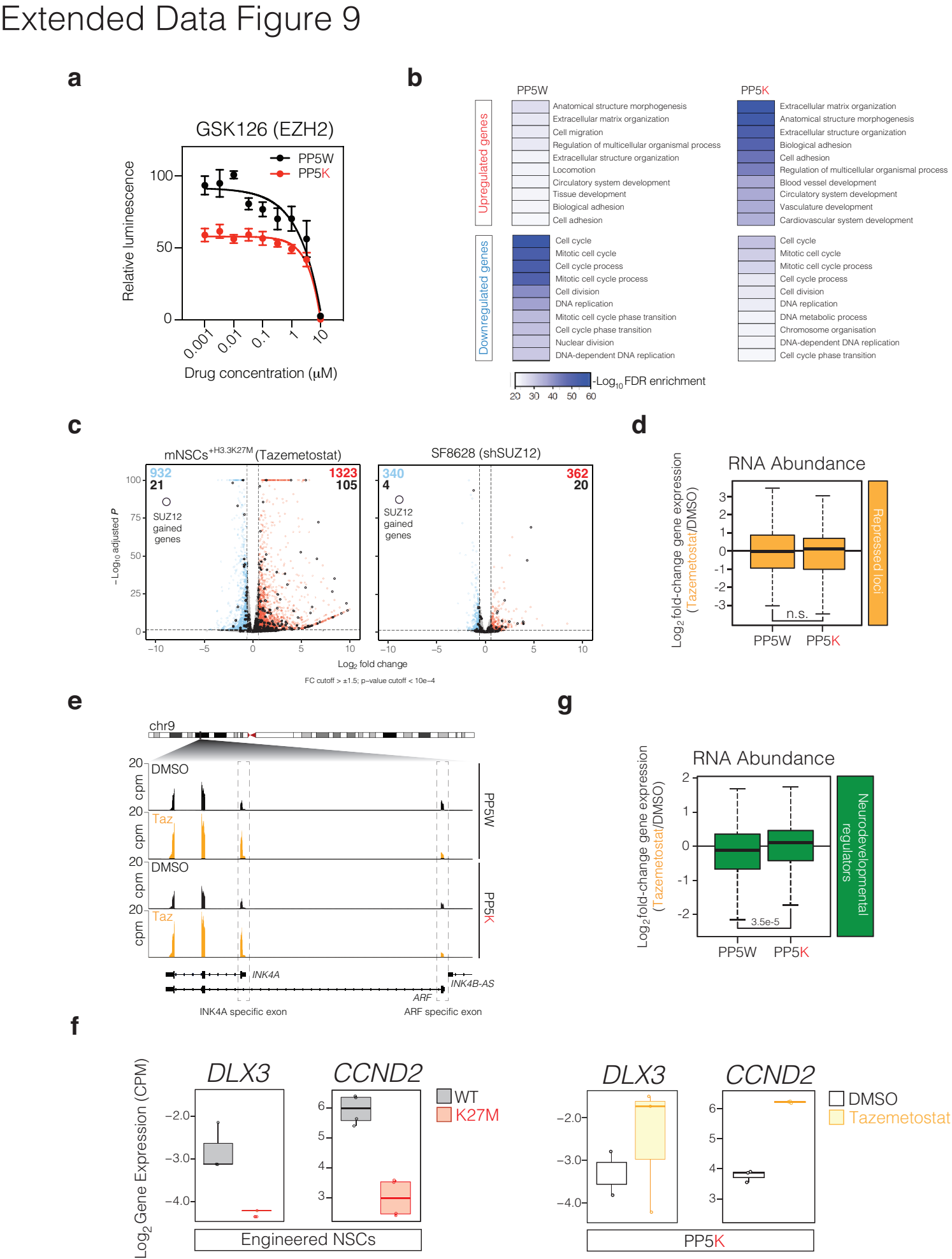

Extended Data Figure 10

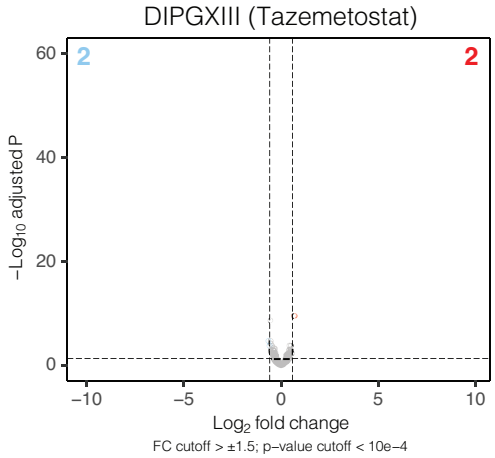

24hrs treatment
2μM Tazemetostat

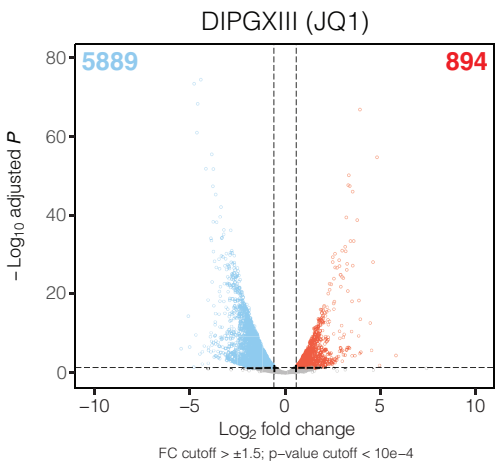

24hrs treatment
1μM JQ1

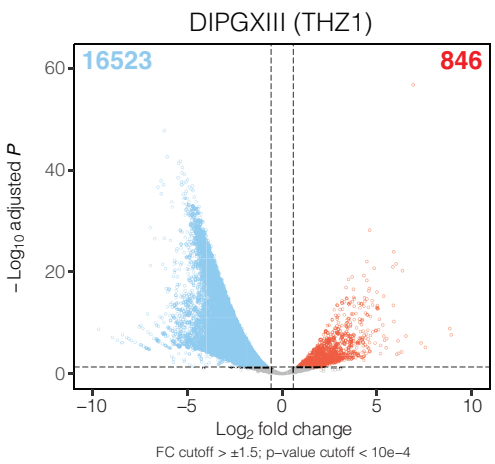

24hrs treatment
0.1μM THZ1

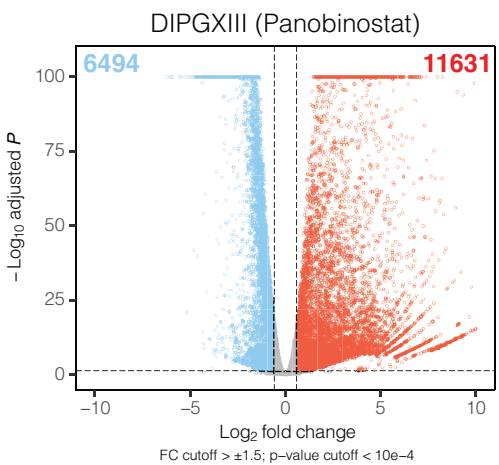

24hrs treatment
0.1μM Panobinostat